



SIMULATION PLATFORM FOR VISION AIDED INERTIAL NAVIGATION

THESIS
SEPTEMBER 2014

Jason Gek Chye Png, Military Expert 5 (Major), Republic of Singapore Air Force

AFIT-ENV-T-14-S-14

**DEPARTMENT OF THE AIR FORCE
AIR UNIVERSITY**

AIR FORCE INSTITUTE OF TECHNOLOGY

Wright-Patterson Air Force Base, Ohio

DISTRIBUTION STATEMENT A.
APPROVED FOR PUBLIC RELEASE; DISTRIBUTION UNLIMITED.

The views expressed in this thesis are those of the author and do not reflect the official policy or position of the United States Air Force, Department of Defense, the United States Government or the corresponding agencies of any other government. This material is declared a work of the U.S. Government and is not subject to copyright protection in the United States.

AFIT-ENV-T-14-S-14

SIMULATION PLATFORM FOR VISION AIDED INERTIAL NAVIGATION

THESIS

Presented to the Faculty

Department of Systems Engineering and Management

Graduate School of Engineering and Management

Air Force Institute of Technology

Air University

Air Education and Training Command

In Partial Fulfillment of the Requirements for the

Degree of Master of Science in Systems Engineering

Jason Gek Chye Png, BS (Hons)

Military Expert 5 (Major), Republic of Singapore Air Force

September 2014

DISTRIBUTION STATEMENT A.

APPROVED FOR PUBLIC RELEASE; DISTRIBUTION UNLIMITED.

SIMULATION PLATFORM FOR VISION AIDED INERTIAL NAVIGATION

Jason Gek Chye Png, BS (Hons)

Military Expert 5 (Major), Republic of Singapore Air Force

Approved:

//Signed//

David R. Jacques, PhD (Chairman)

3 Sep 2014

Date

//Signed//

John F. Raquet, PhD (Member)

2 Sep 2014

Date

//Signed//

Brian G. Woolley, Major, PhD, USAF (Member)

2 Sep 2014

Date

Abstract

Integrated Inertial Navigation System (INS) and Global Positioning System (GPS) solutions have become the backbone of many modern positioning and navigation systems. The Achilles' heel of such systems are their susceptibility to GPS outages. Hence, there has been sustained interest in alternate navigation techniques to augment a GPS/INS system. With the advancement in camera technologies, visual odometry is a suitable technique. As the cost and effort required to conduct physical trials on a visual odometry system is extensive, this research seeks to provide a simulation platform that is capable of simulating different grades of GPS/INS systems under various realistic visual odometry scenarios. The simulation platform also allows standardized data to be tested across different navigation filters. The utility of this simulation platform is demonstrated by a trade study on factors affecting the performance of a GPS/INS system augmented with visual odometry.

Dedicated to my dear wife, for your love and patience. To my son and daughter, for bringing me endless joy and motivation. To my parents and the rest of my family, for your continual support.

Acknowledgments

I would like to thank my thesis committee, Dr David Jacques, Dr John Raquet and Maj Brian Woolley. This thesis would not be possible without your guidance, excellent academic instruction and encouragement.

Jason Png

Table of Contents

	Page
Abstract	iv
Acknowledgments	vi
List of Figures	x
List of Tables	xiii
List of Abbreviations	xiv
I. Introduction	1
1.1 Problem Statement	3
1.2 Scope and Assumptions	3
1.3 Methodology	3
1.4 Thesis Overview	4
II. Literature Review	5
2.1 Mathematical Notation	5
2.2 World Geodetic System 1984	6
2.3 Reference Frames	7
2.3.1 Inertial Frame	7
2.3.2 Earth Centered Earth Fixed Frame	7
2.3.3 Navigation Frame	7
2.3.4 Body Frame	8
2.3.5 Sensor Frame	8
2.4 Coordinate Transformations	10
2.4.1 Euler Angle	10
2.4.2 Direction Cosine Matrix	10
2.5 Visual Navigation	11
2.5.1 Identifying Features in an Image	11
2.5.2 Matching Features between Images	11
2.5.3 Estimating the Rotation and Direction of Translation of the Sensor	12
2.6 Kalman Filter	14
2.7 Related Research	17
2.7.1 Integration of Visual Odometry with INS	17
2.7.2 Building Simulation Platform	17
2.8 Summary	18

	Page
III. Methodology	19
3.1 Requirements for the Simulation Platform	19
3.2 Design of Simulation Platform.....	19
3.2.1 Simulate Inertial Measurement Unit.	22
3.2.2 Simulation of Matched Features.	25
3.2.3 Simulate GPS Pseudorange.....	27
3.3 Error Model and Measurement Model for VINS	31
3.3.1 INS Error Model.....	31
3.3.2 GPS Error Model.....	33
3.3.3 Image Measurement Model.....	34
3.3.4 GPS Measurement Model.	36
3.3.5 Overall Measurement Model.....	37
3.4 Verification of Simulation Platform.....	37
3.5 Summary	38
IV. Analysis and Results.....	39
4.1 Scenarios for Trade Study	39
4.1.1 Scenario 2.....	39
4.1.2 Scenario 6.....	40
4.1.3 Scenario 7.....	40
4.2 Results from Trade Study.....	50
4.2.1 Accuracy of a Nominal VINS.	52
4.2.2 Interval between Update.....	54
4.2.3 IMU Quality.	55
4.2.4 Quality of Camera.	59
4.2.5 Camera Pointing Direction.....	63
4.2.6 Method of Calculating Direction of Translation.	65
4.2.7 GPS Clock.....	67
4.2.8 Number of Pseudorange Measurements.....	68
4.3 Conclusion from Trade Study	72
4.4 Summary	72
V. Conclusions and Recommendations	73
5.1 Conclusions of Research	73
5.2 Significance of Research.....	74
5.3 Recommendations for Future Research	74
5.3.1 Alternate Filter Implementation.	74
5.3.2 Implement Delayed State Update Equation.	74
5.3.3 Using Design of Experiment for Trade Space Analysis.	75
5.3.4 Implement Altitude Aiding.	75

	Page
Bibliography	76

List of Figures

	Page
Figure 1. Inertial, ECEF and Navigation (NED) Frames from (M. J. Veth, 2006)	8
Figure 2. Body Frame from (M. J. Veth, 2006).....	9
Figure 3. Sensor (Camera) Frame from (M. J. Veth, 2006).....	9
Figure 4. Epipolar Geometry from (J. Raquet, 2014)	13
Figure 5. Use Case Diagram for VINS Simulation Platform.....	21
Figure 6. Top Level Design of VINS Simulation Platform	21
Figure 7. IDEF0 Diagram Illustrating Simulation of Inertial Measurement Unit	23
Figure 8. Simulation of $\Delta\theta$ from Commercial Inertial Measurement Unit.....	24
Figure 9. Simulation of ΔV from Commercial Inertial Measurement Unit.....	24
Figure 10. IDEF0 Diagram Illustrating Simulation of Matched Features	25
Figure 11. Feature Matching for 9 Successive Pairs of Images.....	26
Figure 12. Sample Output from Simulation Showing Location of Matched Features	27
Figure 13. IDEF0 Diagram Illustrating Simulation of GPS Pseudorange	29
Figure 14. Simulated Crystal Clock Error for GPS Receiver	30
Figure 15. Sample Output Showing Simulation of GPS Pseudorange	30
Figure 16. True Horizontal Trajectory (Scenario 2)	41
Figure 17. True Altitude (Scenario 2).....	41
Figure 18. Number of Matched Features Found from Scenario 2 Side Camera Images..	42
Figure 19. Number of Matched Features Found from Scenario 2 Front Camera Images.	43
Figure 20. True Horizontal Trajectory (Scenario 6)	44

	Page
Figure 21. True Altitude (Scenario 6).....	44
Figure 22. Number of Matched Features Found from Scenario 6 Side Camera Images. .	45
Figure 23. Number of Matched Features Found from Scenario 6 Front Camera Images.	46
Figure 24. True Horizontal Trajectory (Figure 7).....	47
Figure 25. True Altitude (Scenario 7).....	47
Figure 26. Number of Matched Features Found from Scenario 7 Side Camera Images. .	48
Figure 27. Number of Matched Features Found from Scenario 7 Front Camera Images.	49
Figure 28. Position Errors of Nominal VINS Configuration.....	53
Figure 29. Velocity Errors of Nominal VINS Configuration	53
Figure 30. Comparison of Trajectories among Different Grades of IMU.	56
Figure 31. Comparison of Position Error (Commercial IMU vs Tactical IMU)	57
Figure 32. Comparison of Velocity Error (Commercial IMU vs Tactical IMU).....	57
Figure 33. Comparison of Position Error (Commercial IMU vs Navigation IMU)	58
Figure 34. Comparison of Velocity Error (Commercial IMU vs Navigation IMU).....	58
Figure 35. Image Measurement Noise of VINS	60
Figure 36. Comparison of Trajectories among Different Camera Quality	60
Figure 37. Comparison of Position Error (2 Pixel Noise vs 0 Pixel Noise)	61
Figure 38. Comparison of Velocity Error (2 Pixel Noise vs 0 Pixel Noise).....	61
Figure 39. Comparison of Position Error (2 Pixel Noise vs 4 Pixel Noise)	62
Figure 40. Comparison of Velocity Error (2 Pixel Noise vs 4 Pixel Noise).....	62
Figure 41. Comparison of Trajectories between Camera Pointing Directions (Scenario 2)	64

	Page
Figure 42. Comparison of Trajectories between Camera Pointing Directions (Scenario 6)	64
Figure 43. Comparison of Trajectories between Camera Pointing Directions (Scenario 7)	64
Figure 44. Comparison of Trajectories among Different Number of Pseudorange Measurements	69
Figure 45. Comparison of Position Error (2 Pseudoranges vs 1 Pseudorange)	70
Figure 46. Comparison of Velocity Error (2 Pseudoranges vs 1 Pseudorange)	70
Figure 47. Comparison of Position Error (2 Pseudoranges vs 3 Pseudoranges)	71
Figure 48. Comparison of Velocity Error (2 Pseudoranges vs 3 Pseudoranges).....	71

List of Tables

	Page
Table 1. Requirements for Vision-aided Inertial Navigation Simulaton Platform	20
Table 2. Parameters used for different INS Grades (FOGM time constant, $\tau = 3600s$) (Kauffman et al., 2011)	23
Table 3. Typical Allan Variance Parameters for Various Timing Standards (Brown & Hwang, 1992).....	29
Table 4. Parameters Examined in Trade Study.....	50
Table 5. Configurations of Test Cases	51
Table 6. Accuracy of a nominal VINS.....	52
Table 7. Effects of Interval between Updates on Accuracy of Position	54
Table 8. Effects of Grade of IMU on Accuracy of Position	55
Table 9. Effects of Grade of IMU on Accuracy of Position (with Image Measurements and without Image Measurements)	55
Table 10. Effects of Quality of Camera on Accuracy of Position	59
Table 11. Effects of Camera Pointing Direction on Accuracy of Position.....	63
Table 12. Effects of Method of Calculating Direction of Translation on Accuracy of Position	66
Table 13. Number of Invalid Translation and Rotation with ‘Cal t and R’	66
Table 14. Effects of Type of GPS Receiver Clock on Accuracy of Position (With Image and 2 Pseudorange Measurements).....	67
Table 15. Effects of Type of GPS Receiver Clock on Accuracy of Position (With 2 Pseudorange Measurements)	67
Table 16. Effects of Number of Pseudoranges on Accuracy of Position.....	68
Table 17. Effects of Number of Pseudoranges on Accuracy of Position (with Image Measurements and without Image Measurements).....	69

List of Abbreviations

ASPN	All Source Positioning Navigation
DCM	Direction Cosine Matrices
DMRS	Distance Root Mean Square
ECEF	Earth Centered Earth Fixed
FOGM	First-Order Gauss-Markov
GPS	Global Positioning System
IMU	Inertial Measurement Unit
INS	Inertial Navigation System
MEMS	Micro-Electro Mechanical System
PVA	Position, Velocity and Attitude
SIFT	Scale Invariant Feature Transform
SLAM	Simultaneous Localization and Mapping
SVD	Singular Value Decomposition
VINS	Vision-aided Inertial Navigation System
WGN	White Gaussian Noise
WGS	World Geodetic System
ZUPT	Zero Velocity Update

SIMULATION PLATFORM FOR VISION AIDED INERTIAL NAVIGATION

I. Introduction

Inertial navigation is an independent navigation system in which measurements provided by accelerometers and gyroscopes are used to determine the Position, Velocity and Attitude (PVA) of a vehicle relative to a known starting condition. It is used in a wide range of navigation applications in aircraft, spacecraft, land vehicles and ships. Advances in micro-electro mechanical systems (MEMS) technology have made it possible for small and light Inertial Navigation Systems (INS) to be used in small and low-cost vehicles.

The advantage of an INS is that it requires no external reference to determine its position, velocity or attitude once it has been initialized. Hence, an INS is immune to jamming and deception. However, all INS suffer from integration drift as small errors in the measurement of acceleration and angular velocity are integrated into larger errors in position, velocity and attitude. Since the new position is derived from the previous calculated position, and due to the dynamics of the errors with an INS, these errors accumulate quickly as the time since initialization grows. Therefore, the position must be periodically corrected by some other type of navigation system. One of the best sources of measurements for position come from the Global Positioning System (GPS).

The GPS is a system of satellites that transmits signals to receivers on or above the Earth's surface. The receivers can determine their own position if four or more satellites are visible to the receiver. GPS is highly accurate, does not drift over time, has a low cost to implement and is available in real-time. Hence, position measurements from

GPS are suitable for updating an INS. The integration of GPS and INS allows the overall system to perform at levels which are difficult to attain with either sensor alone (M. Veth & Raquet, 2007).

An inherent weakness of a GPS or GPS/INS system is the unavailability of GPS signals in environments that do not have a clear line of sight to the sky, such as urban canyons, indoors or underground. It is also possible for a GPS signal to be jammed. This weakness motivates the development of alternate navigation systems that can work in environments with GPS outages, and in particular for small, low-cost vehicles. One such alternate navigation system is vision-aided inertial navigation. This has become practical as inertial measurement units and cameras are becoming less expensive, smaller, and more reliable with improved processing capabilities. Hence, vision-aided inertial navigation can be applied in small, low-cost vehicles which need to operate in environments with GPS outages.

As the development of a vision-aided inertial navigation system (VINS) requires a significant amount of effort for performance tuning, verification and validation, it would be beneficial to test the design of the system in various simulated environments prior to physical testing of the system in a real environment. Such simulations allow researchers, to focus on the design of navigation filters for a VINS while eliminating hardware and data synchronization problems. This research is in support of a Project Agreement between the United States and Singapore, entitled “GPS/Inertial/Vision Integrated Navigation System (GIVINS)”.

1.1 Problem Statement

This research aims to (1) build a platform that can be used to simulate a VINS operating in an environment with limited GPS signals, and (2) to demonstrate the utility of the platform by using it to study the effects of key design parameters on the performance of a VINS. This simulation platform will then facilitate future research in the development of VINS.

1.2 Scope and Assumptions

The scope of this research is to build a platform to simulate a VINS and to demonstrate the utility of the platform by performing a trade study on a low-cost VINS. The design of a navigation algorithm for the simulated VINS is limited to methods currently available in literature. The simulation platform is currently using real-world images and PVA data collected from a ground vehicle as part of the All Source Positioning Navigation (ASPN) program.

1.3 Methodology

The first part of this research focuses on building a simulation platform and verifying its operation and performance. The second part of this research demonstrates the utility of the platform by examining how various key design parameters of a VINS (such as Measurement Rate, INS Quality, Camera Quality, and Camera Pointing Direction) affects its performance. Three types of observations are utilized in the navigation filter: Limited (0 to 3) GPS pseudorange measurements, image derived measurements (rotation and direction of translation), and inertial measurements (specific forces and angular velocities).

1.4 Thesis Overview

Chapter 2 presents background knowledge essential for this thesis. This includes descriptions of reference frames used for navigation, transformation between these reference frames, the concept of vision aided navigation and Kalman Filters. It will also present related research in the field of vision navigation and simulation of navigation systems. Chapter 3 explains how the simulation platform is built and how its operation and performance is verified. Chapter 4 presents analysis of a VINS trade space carried out using the simulation platform. Chapter 5 concludes this research and proposes potential future works based on the insights gained.

II. Literature Review

This chapter presents the background knowledge required to complete this thesis. The first portion of this chapter begins by defining the standard mathematical notation which is used throughout the thesis. Next, reference frames used for navigation and a mathematical technique for transforming coordinates between these reference frames are defined. This is followed by the concept of visual navigation. Lastly, a brief overview of Kalman filter theory is presented. The second portion of this chapter describes research that is closely related to what this thesis aims to achieve.

2.1 Mathematical Notation

The following mathematical notation is used in this thesis:

- **Scalars:** Scalars are signified by a lower or upper-case case variables in italics (e.g., x).
- **Vectors:** Vectors are by default given in column form and represented using lower-case bold letters (e.g., \mathbf{x}).
- **Matrices:** Matrices are represented using uppercase bolded letters (e.g., \mathbf{X}).
- **Vector Transpose:** The vector (or matrix) transpose is identified by a superscript Roman T, as in \mathbf{x}^T .
- **Estimated Variables:** Variables which are estimates of random variables are denoted by the *hat* character, as in \hat{x} .
- **Direction Cosine Matrices:** Direction cosine matrices used to transform vectors from coordinate frame a to coordinate frame b are denoted by \mathbf{C}_a^b .

2.2 World Geodetic System 1984

As the platform simulates the PVA of a vehicle moving on or near the surface of the Earth, a model of the Earth is required. This research uses parameters defined in the World Geodetic System 1984 (WGS-84) to model the geometry of the Earth (National Imagery and Mapping Agency, 2004). With this model, the position of any point on or near the Earth's surface can be described using a geodetic latitude (φ), longitude (λ) and altitude (h). The rates at which the latitude and longitude change as a vehicle moves on or near the surface of the Earth is governed by the normal and meridian radii (Noureldin, Karamat, & Georgy, 2013). These radii are also used to convert geodetic latitude and longitude to a local-level navigation frame. The normal radius, R_N , is defined for the east-west direction as shown in Eq (1).

$$R_N = \frac{a}{(1 - e^2 \sin^2 \varphi)^{\frac{3}{2}}} \quad (1)$$

where

$$a = 6,378,137.0 \text{ m (WGS-84 semi-major axis)}$$

$$e = 0.08181919 \text{ (WGS-84 ellipsoid eccentricity).}$$

The meridian radius, R_M , is defined for the north-south direction as shown in Eq (2).

$$R_M = \frac{a (1 - e^2)}{(1 - e^2 \sin^2 \varphi)^{\frac{3}{2}}} \quad (2)$$

The rate of change of latitude and longitude are as shown in Eq (3) and (4) respectively.

$$\dot{\varphi} = \frac{v_n}{R_M + h} \quad (3)$$

$$\dot{\lambda} = \frac{v_e}{(R_N + h) \cos \varphi} \quad (4)$$

2.3 Reference Frames

This section describes reference frames that are used to express the PVA of a vehicle. It also includes transformations between these reference frames.

2.3.1 Inertial Frame.

The inertial reference frame, denoted by x^i, y^i and z^i in Figure 1, originates at the center of the earth with the vertical z axis passing through the North Pole. The x axis points in an arbitrarily chosen direction that remains fixed in orientation relative to the rotating earth and together with the y axis completes a right handed Cartesian coordinate system.

2.3.2 Earth Centered Earth Fixed Frame.

The earth centered earth fixed frame (ECEF) reference frame, denoted by x^e, y^e and z^e in Figure 1, is initially aligned with the inertial frame and rotates about the z^e axis at the earth sidereal rate. The x axis projects through the prime meridian at the equator, and the y axis completes the right handed Cartesian coordinate system.

2.3.3 Navigation Frame.

The navigation frame, denoted by x^n, y^n and z^n in Figure 1, has its origin located at a predefined point on a vehicle. It is also known as the local-level frame as the x, y , and z -axes are aligned to the locally level North, East and Down (NED) directions, respectively. There is another commonly used navigation frame that differs from the NED frame, whereby the x, y , and z -axes are aligned to the locally level East, North and Up (ENU) directions, respectively. The NED frame is used for most part of this thesis. A distinction will be made when the ENU frame is used.

2.3.4 Body Frame.

The body frame, denoted by x^b , y^b and z^b in Figure 2, is an orthonormal basis, rigidly attached to the vehicle with origin co-located with the navigation frame. The x , y , and z -axes point out the nose, right-wing/door, and bottom of a vehicle respectively.

2.3.5 Sensor Frame.

The sensor frame or camera frame, as denoted by x^c , y^c and z^c in Figure 3, has its origin at the sensor's optical center. The x and y axes point up and to the right, respectively, and are parallel to the image plane of the sensor. The z axis points out of the sensor perpendicular to the image plane.

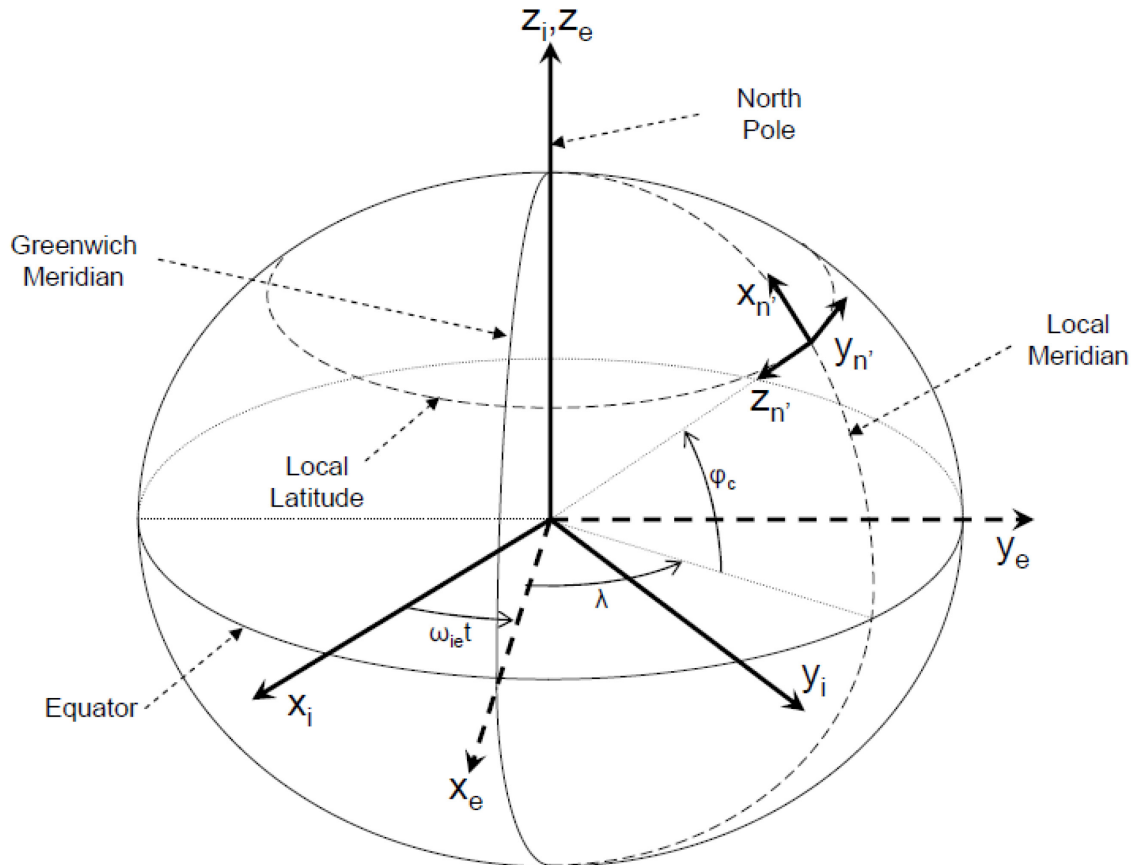


Figure 1. Inertial, ECEF and Navigation (NED) Frames from (M. J. Veth, 2006)

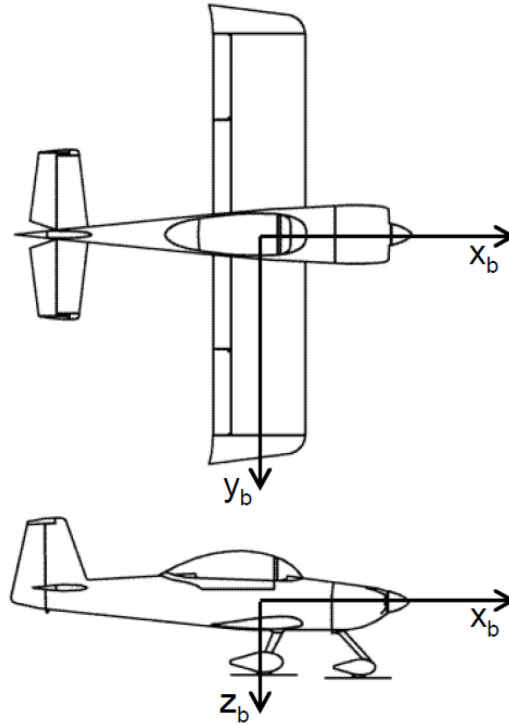


Figure 2. Body Frame from (M. J. Veth, 2006)

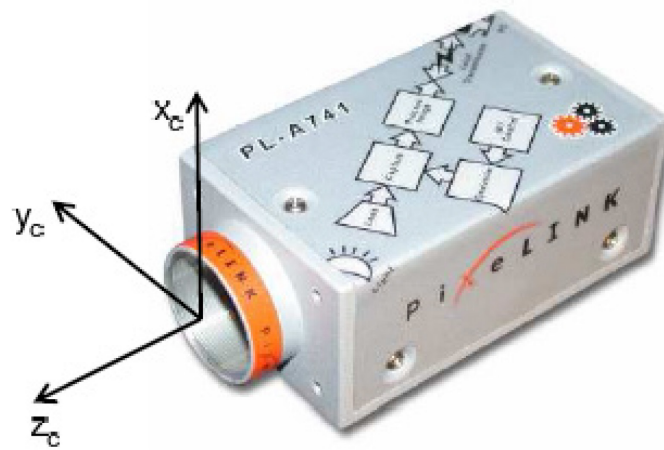


Figure 3. Sensor (Camera) Frame from (M. J. Veth, 2006)

2.4 Coordinate Transformations

Coordinate transformations describe the relationships between vectors expressed in various reference frames. For the purposes of this thesis, the relevant transformations are Euler angles and direction cosine matrices (DCM).

2.4.1 Euler Angle.

Euler angles are elements of a three-component vector corresponding to a specific sequence of single-axis rotations to rotate from one reference frame to another. A common application of Euler angles is expressing the transformation from the body to navigation frame of a vehicle as a roll (ϕ), pitch (θ) and yaw angle (ψ).

2.4.2 Direction Cosine Matrix.

Direction cosine matrices are four-parameter transformations expressed as a 3 x 3 matrix. The matrix consists of the inner product (or cosines) of each unit basis vector in one frame with each unit basis vector in another frame. The matrix form of the direction cosine is convenient for transforming vectors, as in Eq (5), where a vector expressed in frame a is rotated to frame b by multiplying it with a DCM.

$$\mathbf{p}^b = \mathbf{C}_a^b \mathbf{p}^a \quad (5)$$

The DCM has the following properties when it is used to transform right-hand Cartesian coordinates

$$\text{Det}(\mathbf{C}_a^b) \equiv |\mathbf{C}_a^b| = 1 \quad (6)$$

$$\mathbf{C}_b^a = (\mathbf{C}_a^b)^{-1} = (\mathbf{C}_a^b)^T \quad (7)$$

$$\mathbf{C}_a^c = \mathbf{C}_b^c \mathbf{C}_a^b \quad (8)$$

2.5 Visual Navigation

This section describes the key processes in visual odometry. It begins with the identification of features in an image. This is followed by matching features between the images. Finally, the movement (rotation and direction of translation) of the sensor can be estimated using epipolar constraints.

2.5.1 Identifying Features in an Image.

A feature refers to a location in an image that is distinct in some manner. There are many techniques to detect features in an image. These techniques are commonly classified into their principles for detection, such as edge detection, corner detection, blob detection, and feature description. The technique used in this thesis to identify a feature is the Scale Invariant Feature Transform (SIFT) developed by Lowe (Lowe, 1999). This technique works using the principle of feature description. As the SIFT features are unaffected by scaling, orientation, and mostly unaffected by lighting and affine distortion, it is ideal for detecting features in moving images, and the features are suitable for tracking. SIFT identifies image features that have the characteristics described above by using Gaussian blurring to identify features that are maximum/minimum in scale space. Descriptors that uniquely describe these features are then formed. More details can be found in (Lowe, 1999) and (Lowe, 2004).

2.5.2 Matching Features between Images.

As SIFT descriptors uniquely describe features in an image, features with identical or relatively similar descriptors can be considered to be the same. Feature matching identifies corresponding features from a pair of successive images. This process starts by determining the similarity of a feature in the leading image with all the features

in the trailing image. The trailing image feature with the closest similarity is declared to be a match. To remove outliers in the matching process, additional processing, such as verification that the candidate feature is significantly closer than the next closest feature to be matched can be performed. The same process is repeated for the remaining features in the leading image and a list containing only matched features for each successive pair of images is obtained.

2.5.3 Estimating the Rotation and Direction of Translation of the Sensor.

Epipolar geometry refers to the intrinsic projective geometry between two views (Hartley & Zisserman, 2004). It is independent of scene structure, and only depends on the cameras' internal parameters and relative pose. If a point in 3D space is imaged as point \mathbf{x} in the first view and point \mathbf{x}' in the second view, as shown in Figure 4, these points and the camera centers are coplanar. The 3 x 3 Fundamental matrix \mathbf{F} is the algebraic representation of epipolar geometry that satisfies the constraint as shown in Eq (9).

$$\underline{\mathbf{x}}_p'^T \mathbf{F} \underline{\mathbf{x}}_p = 0 \quad (9)$$

where $\underline{\mathbf{x}}_p$ and $\underline{\mathbf{x}}_p'$ are homogeneous pixel coordinates

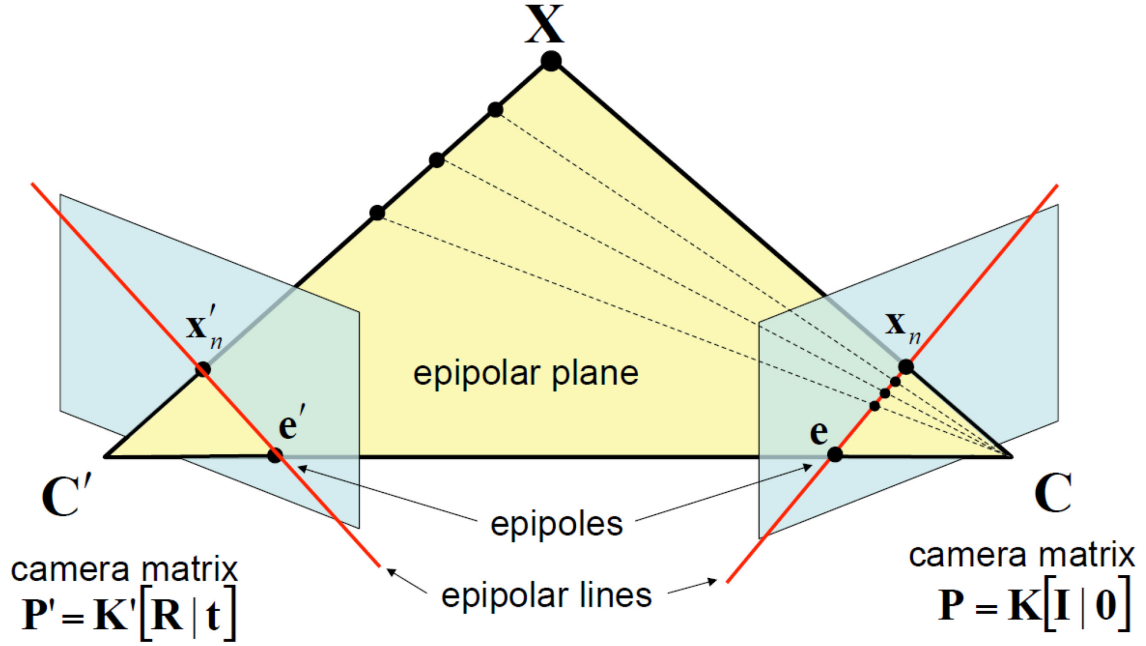


Figure 4. Epipolar Geometry from (J. Raquet, 2014)

The Essential matrix \mathbf{E} also establishes an epipolar constraint. It is related to the Fundamental matrix through the following relationship $\mathbf{E} = \mathbf{K}'^T \mathbf{F} \mathbf{K}$, where the camera calibration matrix \mathbf{K} is defined as shown in Eq (10).

$$\mathbf{K} = \begin{bmatrix} f_c(1) & \alpha_c f_c(1) & c_c(1) \\ 0 & f_c(2) & c_c(2) \\ 0 & 0 & 1 \end{bmatrix} \quad (10)$$

where

$f_c(1), f_c(2)$ = horizontal and vertical focal length

$c_c(1), c_c(2)$ = principal point, or center point of the image plane

α_c = angle between the horizontal and vertical sensor axes.

Hence, the epipolar constraint shown in Eq (9) can be re-written in terms of the Essential matrix as shown

$$\underline{\mathbf{x}}_p'^T * (\mathbf{K}'^T)^{-1} \mathbf{E} \mathbf{K}^{-1} * \underline{\mathbf{x}}_p = 0 \quad (11)$$

$$\underline{\mathbf{x}}_n'^T \mathbf{E} \underline{\mathbf{x}}_n = 0 \quad (12)$$

where $\underline{\mathbf{x}}_n'$ and $\underline{\mathbf{x}}_n$ are homogeneous normalized coordinates of $\underline{\mathbf{x}}_p'$ and $\underline{\mathbf{x}}_p$ respectively.

Hence, given a list of matched features, it is possible to compute the Essential matrix. As the measurements of the matched features are subjected to noise, an exact solution for the Essential matrix is usually not possible. A total least squares approach can be used to estimate an Essential matrix which optimally satisfies the epipolar constraints for the given list of matched features. This approach is commonly known as the eight-point algorithm and a further description can be found in (Longuet-Higgins, 1987). Finally, the rotation and direction of translation of the sensor can be determined by computing the singular value decomposition of the Essential matrix as described by (Hartley & Zisserman, 2004).

2.6 Kalman Filter

The Kalman filter is a recursive algorithm that uses a system model and a stream of noisy measurement updates to produce an optimal (minimum variance) estimate of the system state. This thesis uses the conventional Kalman filter, which assumes a linear system, and that the state and measurement errors can be modelled using zero mean white Gaussian noise (WGN).

In continuous time, the system is modelled in terms of first-order differential equation as shown in Eq (13).

$$\dot{\mathbf{x}}(t) = \mathbf{F}(t)\mathbf{x}(t) + \mathbf{B}(t)\mathbf{u}(t) + \mathbf{G}(t)\mathbf{w}(t) \quad (13)$$

where

$\mathbf{x}(t)$ = system states

$\mathbf{F}(t)$ = state dynamics matrix

$\mathbf{B}(t)$ = input matrix

$\mathbf{u}(t)$ = vector of deterministic inputs

$\mathbf{G}(t)$ = noise distribution matrix

$\mathbf{w}(t)$ = WGN state uncertainty with noise strength $\mathbf{Q}(t)$.

In discrete time, the system is expressed as a state-space model as shown in Eq (14).

$$\mathbf{x}_k = \mathbf{\Phi}_k \mathbf{x}_{k-1} + \mathbf{B}_{k-1} \mathbf{u}_{k-1} + \mathbf{G}_{k-1} \mathbf{w}_{k-1} \quad (14)$$

where

\mathbf{x}_k = discrete states (n x 1)

$\mathbf{\Phi}_k$ = state transition matrix that transform the states from t_{k-1} to t_k
(n x n)

\mathbf{B}_{k-1} = discrete input matrix (n x n)

\mathbf{u}_{k-1} = vector of discrete inputs (n x 1)

\mathbf{G}_{k-1} = discrete noise distribution matrix (n x s)

\mathbf{w}_{k-1} = discrete noise vector with discretized noise strength \mathbf{Q}_d (s x 1).

Given a discrete stochastic system model and initial conditions, the Kalman filter will provide state estimates over time by propagating the states and their covariance as shown in Eq (15) and (16) respectively.

$$\hat{\mathbf{x}}_k^- = \Phi_k \hat{\mathbf{x}}_{k-1} \quad (15)$$

$$\mathbf{P}_k^- = \Phi_k \mathbf{P}_{k-1} \Phi_k^T + \mathbf{Q}_k \quad (16)$$

When there is no measurement, the state continues to propagate and its covariance increases. When a measurement is available, the Kalman gain \mathbf{K}_k is computed as shown in Eq (17). The Kalman gain is used to weight a measurement for incorporation into the Kalman estimate. The optimal state estimate and its covariance are then computed as shown in Eq (18) and (19). The filter will then propagate forward using the updated state estimate until the next measurement is available.

$$\mathbf{K}_k = \mathbf{P}_k^- \mathbf{H}_k^T [\mathbf{H}_k \mathbf{P}_k^- \mathbf{H}_k^T + \mathbf{R}_k]^{-1} \quad (17)$$

$$\hat{\mathbf{x}}_k = \hat{\mathbf{x}}_k^- + \mathbf{K}_k (\mathbf{z}_k - \mathbf{H}_k \hat{\mathbf{x}}_k^-) \quad (18)$$

$$\mathbf{P}_k = (\mathbf{I} - \mathbf{K}_k \mathbf{H}_k) \mathbf{P}_k^- \quad (19)$$

The measurement residual and its covariance are given by Eq (20) and (21). The residual will be zero mean WGN as long as the Kalman filter assumptions are maintained.

$$\text{Residual} = \mathbf{z}_k - \mathbf{H}_k \hat{\mathbf{x}}_k^- \quad (20)$$

$$\text{Measurement Covariance} = \mathbf{H}_k \mathbf{P}_k^- \mathbf{H}_k^T + \mathbf{R}_k \quad (21)$$

2.7 Related Research

This thesis is closely related to two areas of research, namely integration of visual odometry with INS, and building a simulation platform for developing navigation-related systems.

2.7.1 Integration of Visual Odometry with INS.

Over the years, there have been numerous investigations focused on the integration of visual odometry and INS. The methods of gathering data for analysis can be grouped into 3 different categories. The data could be

- Purely simulated (Dae Hee Won, Sukchang Yun, Young Jae Lee, & Sangkyung Sung, 2012; Giebner, 2003),
- Based on real world (Chowdhary, Johnson, Magree, Wu, & Shein, 2013; George & Sukkarieh, 2007; Seong-Baek Kim, Seung-Yong Lee, Tae-Hyun Hwang, & Kyoung-Ho Choi, 2004) , or
- Based on a combination of simulation and real world (M. Veth & Raquet, 2007).

These researchers focused on the algorithms for integrating visual odometry and INS. None of the literature reviewed focused on building a simulation platform using real world data that could be used for developing or evaluating a VINS.

2.7.2 Building Simulation Platform.

There are datasets/simulation platforms that are created from real world data. However, these datasets are used for benchmarking robotics algorithms or Simultaneous Localization and Mapping (SLAM) related problems. For example, Technische Universität München provides a large dataset for the evaluation of visual SLAM systems

in an indoor environment (Technische Universität München, 2014). Robotics Data Set Repository provides a collection of data for the evaluation of robotics algorithms in an indoor environment (University of Southern California Robotics Research Lab, 2011). Rawseeds Project is another collection of data for evaluation and comparison of robotics algorithm (Bonarini et al., 2014). None of these datasets are suitable for the development of VINS in an outdoor environment.

2.8 Summary

In this chapter, the background knowledge required to complete this thesis was discussed. A physical model of the Earth was presented as it was required for simulating real world navigation. Navigation reference frames and methods for rotating coordinates between these reference frames were defined. This was followed by a presentation of the concept of visual odometry. Lastly, a brief overview of Kalman filter theory was presented. Research into the areas closely related to this thesis revealed that no similar work had been done to build a simulation platform for the development of VINS.

III. Methodology

The System Engineering methodology is used for the design approach for the simulation platform. The requirements for the simulation platform are derived from its goal. Conceptual designs of the simulation platform are planned using IDEF0 diagrams. Detailed design leads to the definition, construction and verification of the key components (Matlab functions) in the simulation platform.

3.1 Requirements for the Simulation Platform

The goal of the simulation platform is to be able to facilitate the design of navigation filters for a VINS while eliminating hardware and data synchronization problems. Requirements for the simulation platform were derived from this goal and discussions with the stakeholders/eventual users of the simulation platform. These requirements are broken down as shown in Table 1.

3.2 Design of Simulation Platform

With the requirements derived, the ASPN dataset was studied to determine the design of the simulation platform. The use case diagram of the simulation platform, shown in Figure 5, shows the normal scenario where a user is interacting with the simulation platform. The IDEF0 A-0 diagram, shown in Figure 6, defines the main components of the simulation platform, the inputs and outputs of these components, the control (i.e. algorithms) used in these components and the mechanism (i.e. the program that is used to build the simulation, Matlab). The top level design also shows how these components interact with each other.

Table 1. Requirements for Vision-aided Inertial Navigation Simulaton Platform

No.	Requirement
1	Simulate IMU
1.1	Simulate 3 different grades of IMU (Commercial, Tactical, and Navigation)
1.1.1	<p>The quality of the IMUs is defined by the following parameters:</p> <ul style="list-style-type: none"> - Standard deviation of the time-correlated bias for accelerometer measurements, σ_{accel}. - Time constant of the time-correlated bias for accelerometer measurements, T_{accel}. - Velocity random walk due to accelerometer, VRW - Standard deviation of the time-correlated bias for gyro measurements, σ_{gyro}. - Time constant of the time-correlated bias for gyro measurements, T_{gyro}. - Angular random walk due to gyro, ARW
1.2	Simulate different trajectories using true position, velocity and attitude collected from the ASPN program.
2	Simulate Features
2.1	Simulate realistic feature geometry (i.e. 3D location of features) using photos taken from the ASPN program
2.1.1	Features are detected by a monocular camera
2.1.2	Features are in an outdoor environment
2.1.3	Features are extracted from photos taken in multiples of a 0.25 second interval
2.2	Simulate 2 different camera pointing directions (front, side)
2.3	Simulate varying camera calibration quality
3	Simulate GPS Pseudorange Measurements
3.1	Errors must be added into the GPS pseudorange measurements based on 3 different types of receiver clock (Crystal, Ovenized Crystal, and Rubidium)
3.1.1	<p>The quality of the receiver clock is defined by the following parameters:</p> <ul style="list-style-type: none"> - Clock bias - Clock drift
3.2	Simulate at least 3 pseudorange measurements
3.3	Measurements are simulated from satellites with high elevation
3.4	Capable of simulating different durations of GPS outage
4	User Interface
4.1	All parameters required to run the system must be kept in a single file
4.2	Users should only need to access the parameter file when using the system. They should not need to amend or access other files.

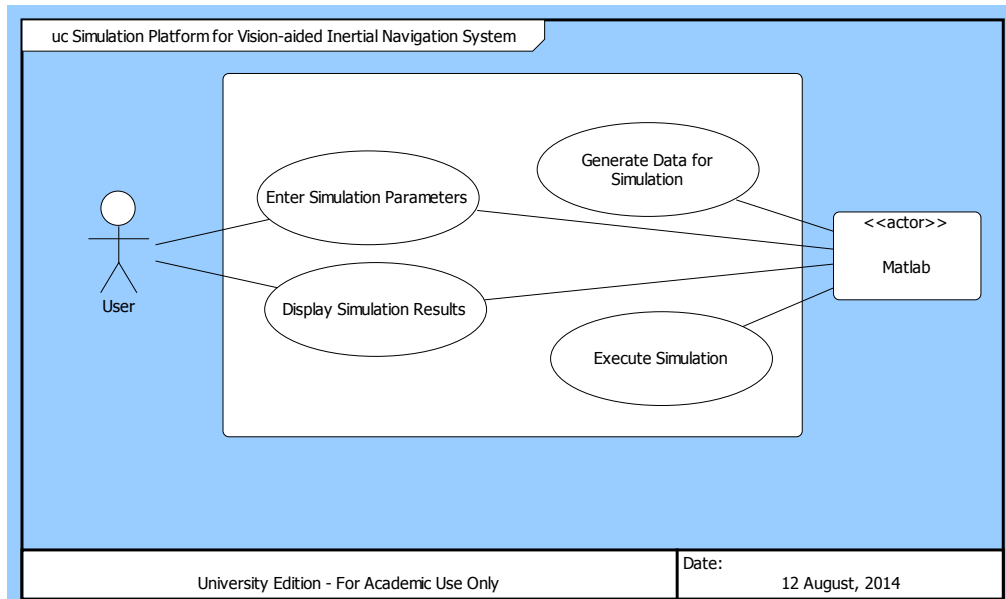


Figure 5. Use Case Diagram for VINS Simulation Platform. It provides a simplified representation of what the simulation platform does. It also shows the user's interaction with the simulation platform, i.e. the user only needs to enter the parameters for simulation, Matlab will generate the data, execute the simulation and display the results to the user.

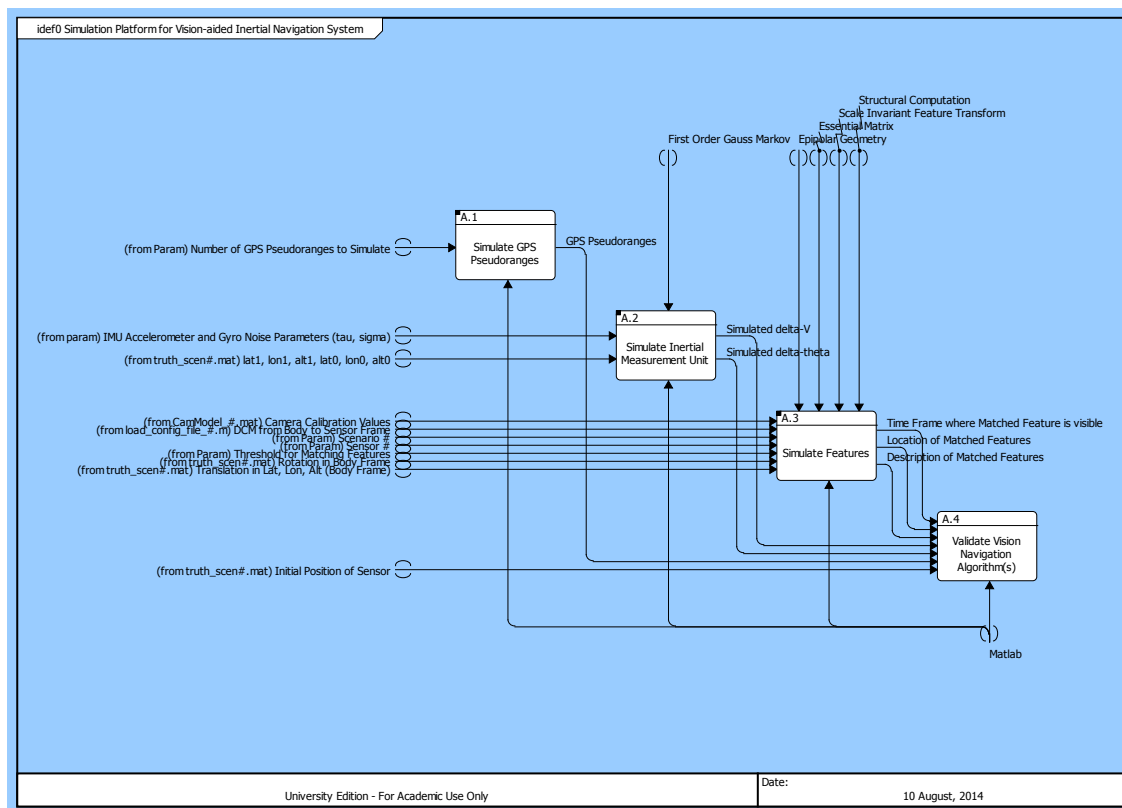


Figure 6. Top Level Design of VINS Simulation Platform

The remaining part of this section describes the design of the various components of the simulation platform.

3.2.1 Simulate Inertial Measurement Unit.

An Inertial Measurement Unit (IMU) measures one of the following (1) specific forces and angular rates, or (2) specific force and angular rate integrated over a time interval. The simulation platform modelled the output of the IMU using the ΔV (specific force integrated over a time interval) and $\Delta\theta$ (angular rate integrated over a time interval). This was simulated by inverting the INS mechanization as shown in Figure 7. Error-free measurements from the IMU were derived using PVA information from the ASPN data. Noise and bias in the gyroscope and accelerometer were added to these error-free measurements to simulate output from any grade of INS (commercial, tactical and navigation). The biases were modelled as first-order Gauss-Markov (FOGM) processes, while the gyroscope and accelerometer noise were modelled as random walk processes. The parameters used for these processes are shown in Table 2. While a real inertial system may include other types of errors, modeling sensor errors as a combination of a random walk and a first order Gauss-Markov bias provide a reasonable approximation of inertial system performance (Kauffman, Morton, Raquet, & Garmatyuk, 2011). Figure 8 and Figure 9 show examples of the simulated $\Delta\theta$ and ΔV measurements from a commercial IMU.

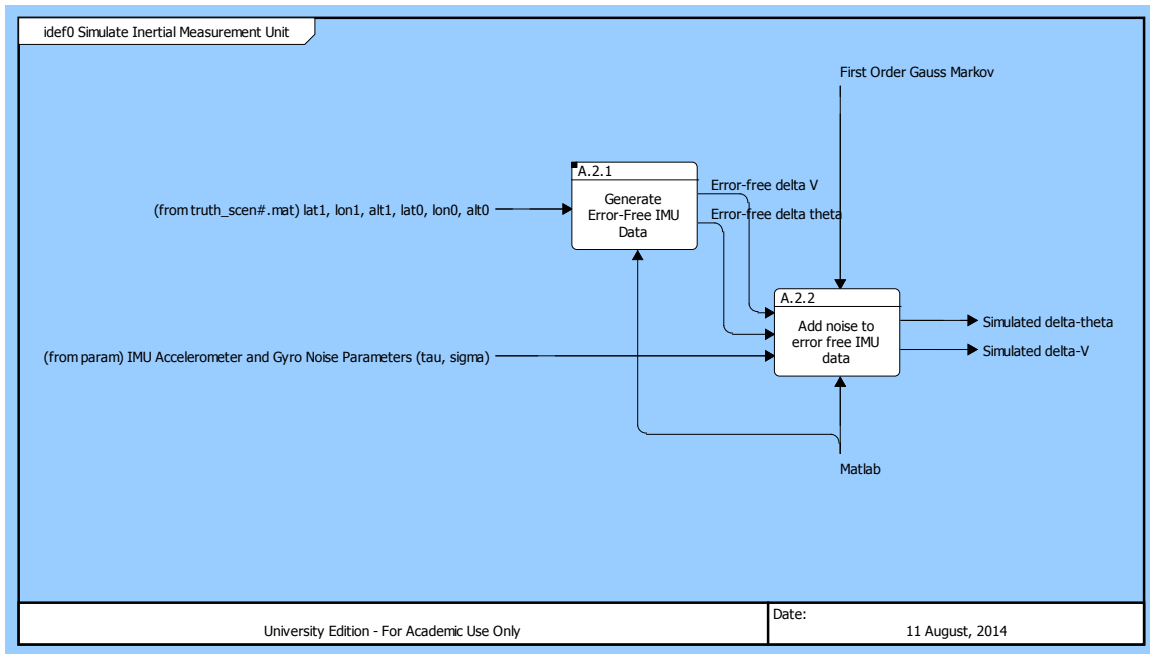


Figure 7. IDEF0 Diagram Illustrating Simulation of Inertial Measurement Unit

Table 2. Parameters used for different INS Grades (FOGM time constant, $\tau = 3600\text{s}$)
(Kauffman et al., 2011)

INS Grade	Accel FOGM σ (m/s^2)	Accel RW σ ($\text{m/s}^{3/2}$)	Gyro FOGM σ (rad/s)	Gyro RW σ ($\text{rad/s}^{1/2}$)
Commercial (Cloudcap Crista)	1.96e-1	4.3e-3	8.7e-3	6.5e-4
Tactical (HG1700)	9.8e-3	9.5e-3	4.8e-6	8.7e-5
Navigation (HG9900 – H764G)	2.45e-4	2.3e-4	7.2e-9	5.8e-7

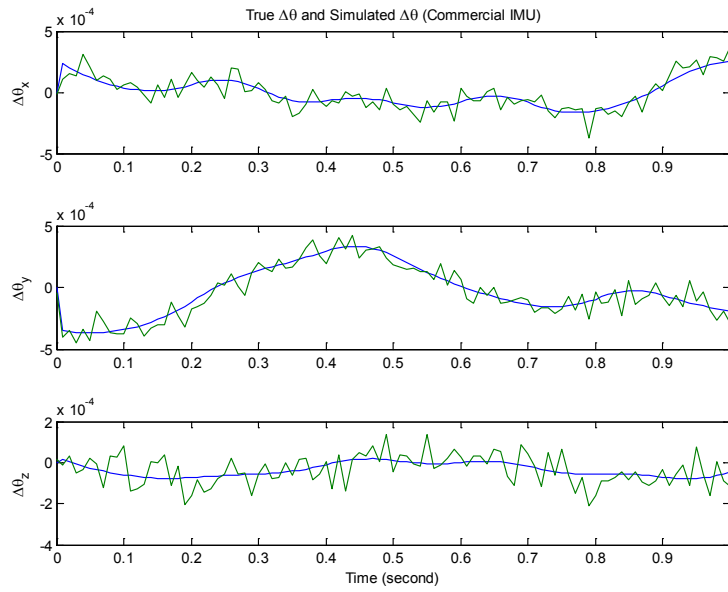


Figure 8. Simulation of $\Delta\theta$ from Commercial Inertial Measurement Unit. The figure shows the results from simulating 1 second of a commercial IMU. The blue lines show the $\Delta\theta$ from an error-free IMU, while the green lines show the $\Delta\theta$ from a simulated commercial IMU.

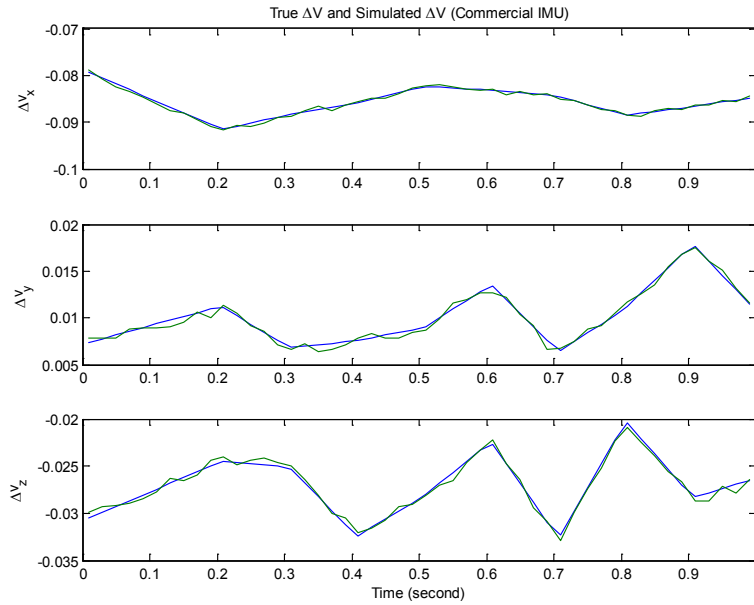


Figure 9. Simulation of ΔV from Commercial Inertial Measurement Unit. The figure shows the results from simulating 1 second of a commercial IMU. The blue lines show the ΔV from an error-free IMU, while the green lines show the ΔV from a simulated commercial IMU.

3.2.2 Simulation of Matched Features.

Matched features for the platform were simulated by reversing the process of visual odometry as shown in Figure 10. Using true PVA information and the set of images from the ASPN data, the rotation \mathbf{R} and translation \mathbf{t} of a sensor's position in a pair of images could be determined. With the rotation and translation data, the Essential matrix relating matched features between the 2 images could be computed using Eq (22).

$$\mathbf{E} = [\mathbf{t}]_x \mathbf{R} \quad (22)$$

where

$[\mathbf{t}]_x$ is the matrix representation of the cross product with \mathbf{t} .

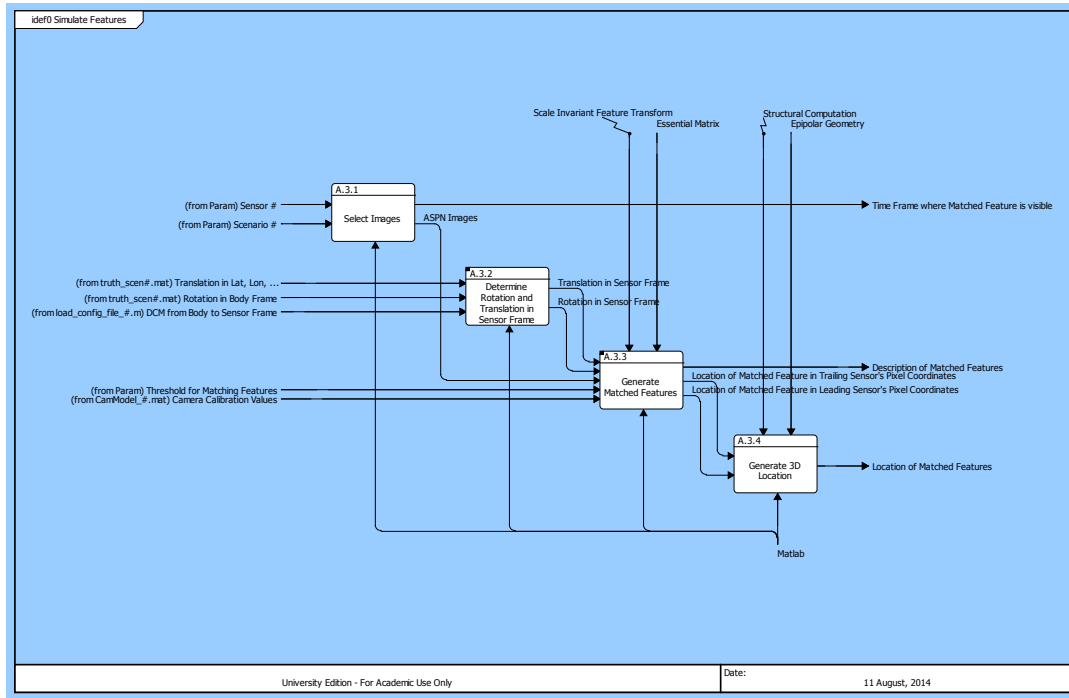


Figure 10. IDEF0 Diagram Illustrating Simulation of Matched Features. Simulation of matched features begins by selecting a pair of photos from the ASPN data (Block A.3.1). Next, the true rotation and translation of the sensor in vehicle frame are retrieved from the ASPN data. The rotation and translation are converted to the sensor frame using the body to sensor DCM (Block A.3.2). This is followed by features matching using SIFT and the Essential matrix (Block A.3.3). Lastly, the 3D position of the matched feature is calculated (Block A.3.4).

The next step involved detecting and matching features between successive pairs of images from the ASPN data using SIFT. First, the Euclidean distance between the SIFT description of the two features is used to determine their similarity. A match is only accepted if its distance is less than a pre-determined ratio times the distance to the second closest match. This pre-determined ratio typically ranges between 0.5 and 0.7. To improve the quality of matches, the Essential matrix found from the previous step was used to filter out bad matches. Features that did not meet the epipolar constraints were eliminated from the list of matched features. Figure 11 shows an example of features matching for 9 successive pairs of images.

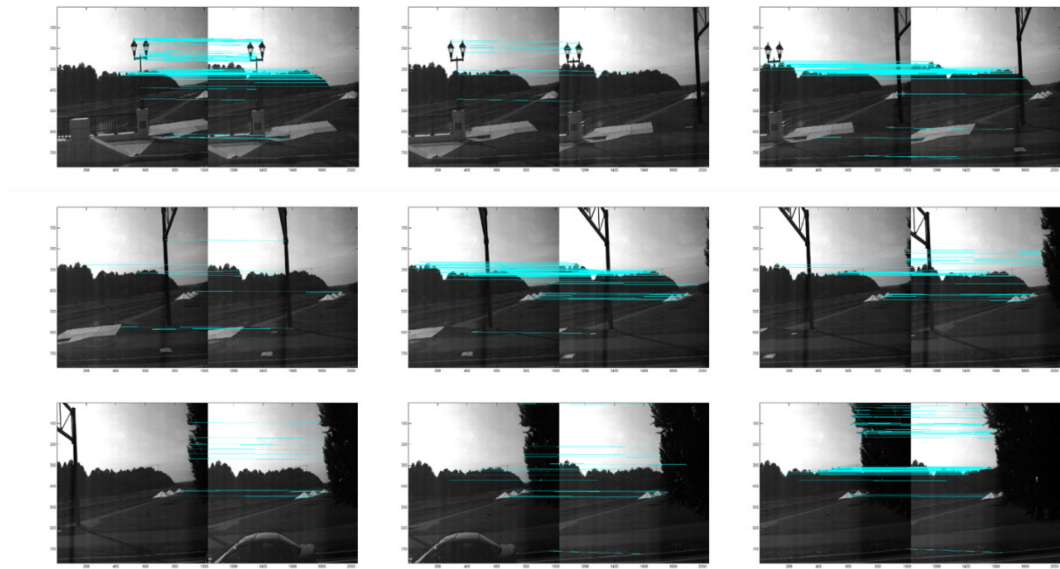


Figure 11. Feature Matching for 9 Successive Pairs of Images

With the list of matched features, the last step in the simulation of matched features was to compute the position of these features in 3D-space given its pixel position in the two images. The method used in this thesis was based on the algorithm found in

(Longuet-Higgins, 1987). Figure 12 depicts a visualization of the features found with respect to the location of the camera.

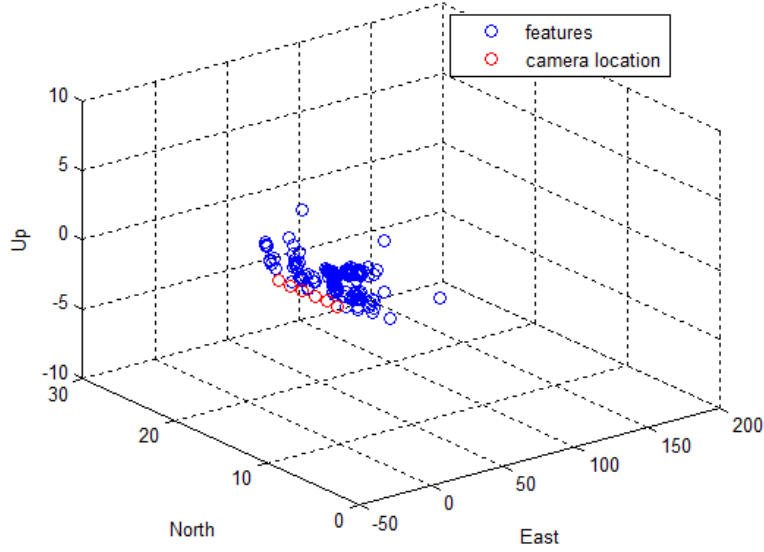


Figure 12. Sample Output from Simulation Showing Location of Matched Features

3.2.3 Simulate GPS Pseudorange.

The pseudorange from a GPS satellite to the GPS receiver can be modelled by Eq (23) as described in (Misra & Enge, 2006).

$$\rho_{GPS}^m = r^m + c\delta t_r - c\delta t_s + cI^m + cT^m + \tilde{\varepsilon}_\rho^m \quad (23)$$

where

ρ_{GPS}^m = measured pseudorange from the m^{th} satellite to the GPS receiver
(meters)

r^m = the actual distance between the receiver antenna at the reception time
and the satellite's antenna at the transmit time (meters)

δt_r = the receiver clock error (sec)

- c = the speed of light (meters/sec)
- δt_s = the satellite clock error (sec)
- I^m = ionospheric delay (sec)
- T^m = tropospheric delay (sec)
- $\tilde{\epsilon}_\rho^m$ = error due to inexact modelling, receiver noise and multipath.

For the simulation platform, only the receiver clock error was used to simulate pseudorange measurement. The satellite clock errors, ionospheric delay, and tropospheric delay were treated as measurement noise in the simulation platform. The process to simulate GPS pseudoranges is shown in Figure 13. First, the position of GPS satellites were calculated using GPS ephemeris data. The true range from the receiver to GPS satellites were then calculated using the true PVA information from the ASPN data. Next, a two-state clock from (Brown & Hwang, 1992) was used to model the receiver clock. It modelled random walk in both the clock bias and drift.

Table 3 shows the parameters values for various timing standards used in the simulation platform. The power of the white noise in the clock bias S_f and drift S_g were determined using Eq (24). Figure 14 shows an example of how errors in a crystal clock accumulate. Finally, this clock error was added to the true range to obtain the simulated pseudorange. Figure 15 shows an example of a simulated pseudorange versus the true range.

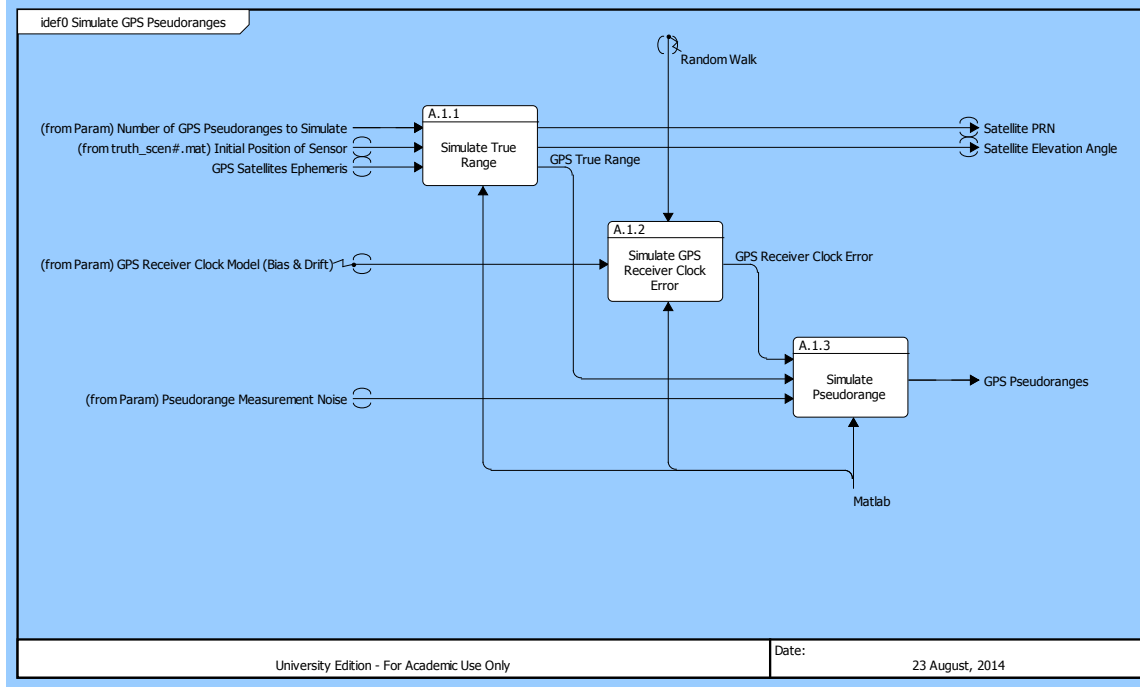


Figure 13. IDEF0 Diagram Illustrating Simulation of GPS Pseudorange

Table 3. Typical Allan Variance Parameters for Various Timing Standards (Brown & Hwang, 1992)

Timing Standard	h_0	h_{-1}	h_{-2}
Crystal	2e-19	7e-21	2e-20
Ovenized Crystal	8e-20	2e-21	4e-23
Rubidium	2e-20	7e-24	4e-29

$$Q = \begin{bmatrix} S_f & 0 \\ 0 & S_g \end{bmatrix} = \begin{bmatrix} 2h_0 & 0 \\ 0 & 8\pi^2 h_{-2} \end{bmatrix} \quad (24)$$

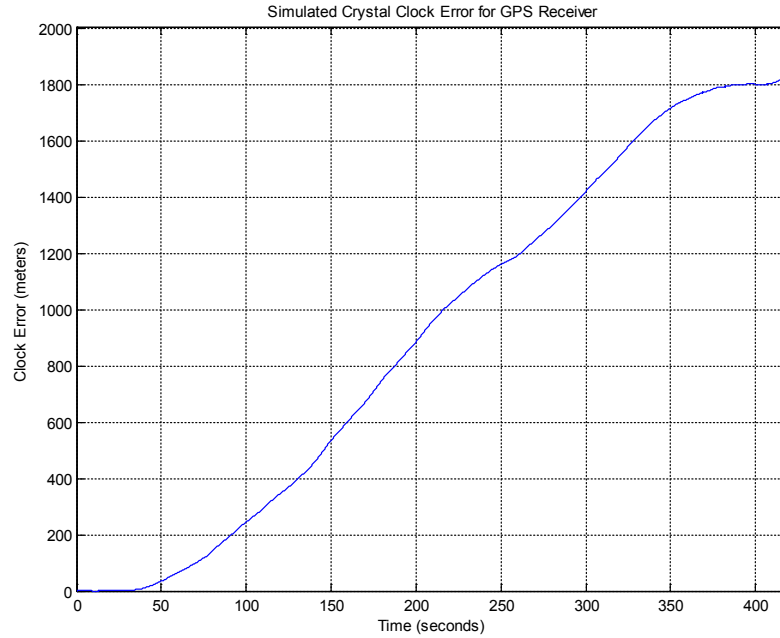


Figure 14. Simulated Crystal Clock Error for GPS Receiver. After 420 seconds, there is an error of approximately 1800m in the GPS pseudorange measurements due to bias and drift in the crystal clock of the GPS receiver.

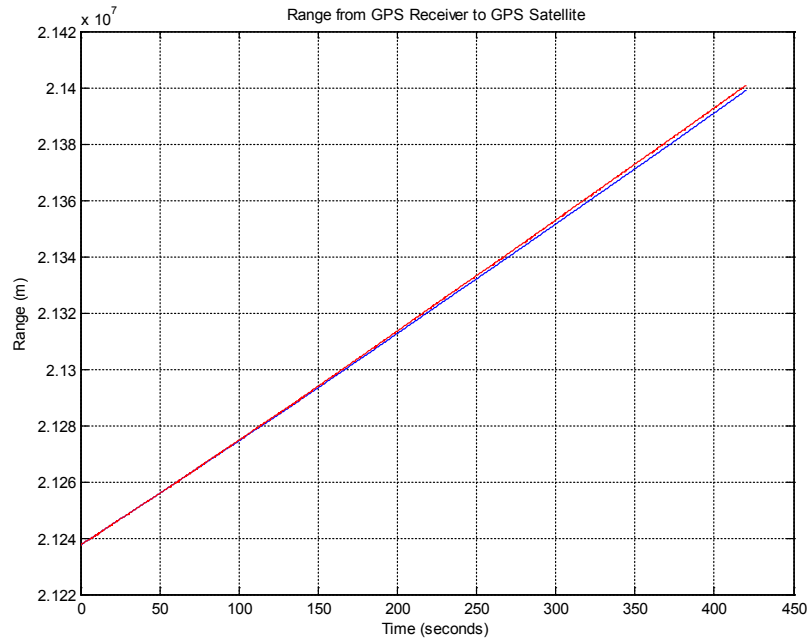


Figure 15. Sample Output Showing Simulation of GPS Pseudorange. The simulated crystal clock error is added to the true range (blue line) to obtain the simulated pseudorange measurement (red line)

3.3 Error Model and Measurement Model for VINS

In order to verify the operation and performance of the simulation platform, an error model integrated with visual odometry and GPS pseudorange measurements was built. The error model makes use of the data generated by the simulation platform to analyze the performance of VINS. It shows how the errors in a navigation system are propagated through the navigation equations.

The error model used in this thesis combined the INS error model with the GPS error model. The overall error model is summarized as shown in Eq (25) and described in the following sub-sections.

$$\begin{bmatrix} \dot{\mathbf{x}}_{\text{INS}} \\ \dot{\mathbf{x}}_{\text{GPS}} \end{bmatrix} = \begin{bmatrix} \mathbf{F}_{\text{INS}} & \mathbf{0} \\ \mathbf{0} & \mathbf{F}_{\text{GPS}} \end{bmatrix} \begin{bmatrix} \mathbf{x}_{\text{INS}} \\ \mathbf{x}_{\text{GPS}} \end{bmatrix} + \begin{bmatrix} \mathbf{G}_{\text{INS}} \\ \mathbf{G}_{\text{GPS}} \end{bmatrix} \mathbf{w} \quad (25)$$

3.3.1 INS Error Model.

The INS error model used in this thesis was built based on the model given in (Noureldin et al., 2013). The errors were modelled by linear state equations and can be represented as shown in Eq (26)

$$\dot{\mathbf{x}}_{\text{INS}} = \mathbf{F}_{\text{INS}} \mathbf{x}_{\text{INS}} + \mathbf{G}_{\text{INS}} \mathbf{w} \quad (26)$$

The state vector, \mathbf{x}_{INS} , consists of position errors, velocity errors, attitude errors and errors in the gyro and accelerometers as shown in Eq (27).

$$\mathbf{x}_{\text{INS}} = \begin{bmatrix} \delta\varphi \\ \delta\lambda \\ \delta h \\ \delta V_e \\ \delta V_n \\ \delta V_u \\ \delta\epsilon_e \\ \delta\epsilon_n \\ \delta\epsilon_u \\ \delta\omega_x \\ \delta\omega_y \\ \delta\omega_z \\ \delta f_x \\ \delta f_y \\ \delta f_z \end{bmatrix} = \begin{bmatrix} \text{Longitude Position Error Estimate (radians)} \\ \text{Latitude Position Error Estimate (radians)} \\ \text{Altitude Position Error Estimate (meters)} \\ \text{East Velocity Error Estimate (m/sec)} \\ \text{North Velocity Error Estimate (m/sec)} \\ \text{Up Velocity Error Estimate (m/sec)} \\ \text{East Axis Tilt Error Estimate (radians)} \\ \text{North Axis Tilt Error Estimate (radians)} \\ \text{Up Axis Tilt Error Estimate (radians)} \\ \text{Gyroscope X Axis Bias Error Estimate} \\ \text{Gyroscope Y Axis Bias Error Estimate} \\ \text{Gyroscope Z Axis Bias Error Estimate} \\ \text{Accelerometer X Axis Bias Error Estimate} \\ \text{Accelerometer Y Axis Bias Error Estimate} \\ \text{Accelerometer Z Axis Bias Error Estimate} \end{bmatrix} \quad (27)$$

The dynamic matrix, \mathbf{F}_{INS} , which propagates errors over time, is shown in Eq (28).

$$\mathbf{F}_{\text{INS}} = \begin{bmatrix} 0 & 0 & 0 & 0 & \frac{1}{R_M + h} & 0 & 0 & 0 & 0 & 0 & 0 & 0 & 0 & 0 & 0 \\ 0 & 0 & 0 & \frac{1}{(R_N + h) \cos \varphi} & 0 & 0 & 0 & 0 & 0 & 0 & 0 & 0 & 0 & 0 & 0 \\ 0 & 0 & 0 & 0 & 0 & 1 & 0 & 0 & 0 & 0 & 0 & 0 & 0 & 0 & 0 \\ 0 & 0 & 0 & 0 & 0 & 0 & 0 & f_u & -f_n & 0 & 0 & 0 & R_{11} & R_{12} & R_{13} \\ 0 & 0 & 0 & 0 & 0 & 0 & -f_u & 0 & f_e & 0 & 0 & 0 & R_{21} & R_{22} & R_{23} \\ 0 & 0 & 0 & 0 & 0 & 0 & f_n & -f_e & 0 & 0 & 0 & 0 & R_{31} & R_{32} & R_{33} \\ 0 & 0 & 0 & 0 & \frac{1}{R_M + h} & 0 & 0 & 0 & 0 & R_{11} & R_{12} & R_{13} & 0 & 0 & 0 \\ 0 & 0 & 0 & -\frac{1}{R_N + h} & 0 & 0 & 0 & 0 & 0 & R_{21} & R_{22} & R_{23} & 0 & 0 & 0 \\ 0 & 0 & 0 & -\frac{\tan \varphi}{R_N + h} & 0 & 0 & 0 & 0 & 0 & R_{31} & R_{32} & R_{33} & 0 & 0 & 0 \\ 0 & 0 & 0 & 0 & 0 & 0 & 0 & 0 & 0 & -\frac{1}{T_g} & 0 & 0 & 0 & 0 & 0 \\ 0 & 0 & 0 & 0 & 0 & 0 & 0 & 0 & 0 & 0 & -\frac{1}{T_g} & 0 & 0 & 0 & 0 \\ 0 & 0 & 0 & 0 & 0 & 0 & 0 & 0 & 0 & 0 & 0 & -\frac{1}{T_g} & 0 & 0 & 0 \\ 0 & 0 & 0 & 0 & 0 & 0 & 0 & 0 & 0 & 0 & 0 & 0 & -\frac{1}{T_a} & 0 & 0 \\ 0 & 0 & 0 & 0 & 0 & 0 & 0 & 0 & 0 & 0 & 0 & 0 & 0 & -\frac{1}{T_a} & 0 \\ 0 & 0 & 0 & 0 & 0 & 0 & 0 & 0 & 0 & 0 & 0 & 0 & 0 & 0 & -\frac{1}{T_a} \end{bmatrix} \quad (28)$$

The noise distribution matrix, \mathbf{G}_{INS} , and its associated WGN are shown in Eq (29) and (30).

$$\mathbf{G}_{\text{INS}} = \begin{bmatrix} \mathbf{0}_{3 \times 12} \\ \mathbf{I}_{12 \times 12} \end{bmatrix} \quad (29)$$

$$\mathbb{E}[\mathbf{w}(t)\mathbf{w}^T(t + \tau)] = \mathbf{Q}_{\text{INS}}\delta(\tau) \quad (30)$$

where

$$\mathbf{Q}_{\text{INS}} = \text{diag} \left[VRW^2, VRW^2, VRW^2, ARW^2, ARW^2, ARW^2, \frac{2\sigma_g^2}{T_g}, \frac{2\sigma_g^2}{T_g}, \frac{2\sigma_g^2}{T_g}, \frac{2\sigma_a^2}{T_a}, \frac{2\sigma_a^2}{T_a}, \frac{2\sigma_a^2}{T_a} \right]$$

3.3.2 GPS Error Model.

Errors in GPS measurements can be modelled by Eq (31).

$$\dot{\mathbf{x}}_{\text{GPS}} = \mathbf{F}_{\text{GPS}}\mathbf{x}_{\text{GPS}} + \mathbf{G}_{\text{GPS}}\mathbf{w} \quad (31)$$

The state vector, \mathbf{x}_{GPS} , consists of the bias and drift of the GPS receiver clock as shown in Eq (32).

$$\mathbf{x}_{\text{GPS}} = \begin{bmatrix} \delta b_r \\ \delta d_r \end{bmatrix} = \begin{bmatrix} \text{Receiver Clock Bias Error Estimate} \\ \text{Receiver Clock Drift Error Estimate} \end{bmatrix} \quad (32)$$

The dynamic matrix, \mathbf{F}_{GPS} , which propagates errors over time is shown in Eq (33). The noise distribution matrix, \mathbf{G}_{GPS} , and its associated WGN are shown in Eq (34) and Eq (35).

$$\mathbf{F}_{\text{GPS}} = \begin{bmatrix} 0 & 1 \\ 0 & 0 \end{bmatrix} \quad (33)$$

$$\mathbf{G}_{\text{GPS}} = \begin{bmatrix} 1 & 0 \\ 0 & 1 \end{bmatrix} \quad (34)$$

$$\mathbb{E}[\mathbf{w}(t)\mathbf{w}^T(t + \tau)] = \mathbf{Q}_{\text{GPS}}\delta(\tau) \quad (35)$$

where

$$\mathbf{Q}_{\text{GPS}} = \begin{bmatrix} S_f & 0 \\ 0 & S_g \end{bmatrix}$$

3.3.3 Image Measurement Model.

In this thesis, measurements from visual odometry were integrated with INS in the form of a 2-dimensional zero velocity update (ZUPT). The concept of a 2D ZUPT is based on the premise that at any time instance, a vehicle is travelling in only one direction. Hence it has zero velocities the two directions orthogonal to the direction of travel. With the direction of travel derived from visual odometry, the zero velocity vectors were determined by finding the orthonormal basis for the null space of the direction of travel. In this research, this was done by performing a Singular Value Decomposition (SVD) on the direction of travel. For example, if the direction of travel, \mathbf{t}_{enu} , was as shown in Eq (36)

$$\mathbf{t}_{\text{enu}} = \begin{bmatrix} 0.0555 \\ 0.9971 \\ -0.0519 \end{bmatrix} \quad (36)$$

Using a SVD, the direction of travel could be expressed as shown in Eq (37)

$$\mathbf{t}_{\text{enu}} = \mathbf{U}\mathbf{S}\mathbf{V}^T = \begin{bmatrix} 0.0555 & -0.9971 & 0.0519 \\ 0.9971 & 0.0581 & 0.0491 \\ -0.0519 & 0.0491 & 0.9974 \end{bmatrix} \begin{bmatrix} 1 \\ 0 \\ 0 \end{bmatrix} [1]^T \quad (37)$$

where \mathbf{U} is a unitary matrix where the columns are the left-singular vectors of \mathbf{t}_{enu} .

The null vector which was cross-tracked to the direction of travel was chosen to be the first null vector, $\mathbf{n}_{1, \text{enu}}$. The null vector in the vertical direction was chosen to be the second null vector, $\mathbf{n}_{2, \text{enu}}$, as shown in Eq (38).

$$\mathbf{n}_{1, \text{enu}} = \begin{bmatrix} -0.9971 \\ 0.0581 \\ 0.0491 \end{bmatrix} \text{ and } \mathbf{n}_{2, \text{enu}} = \begin{bmatrix} 0.0519 \\ 0.0491 \\ 0.9974 \end{bmatrix} \quad (38)$$

Although the ZUPT measurements should be incorporated using delayed-state update equations, the computation in this thesis was simplified by using average measurements in the update equations. Eq (39) to (41) shows how the image measurements and the measurement matrix, \mathbf{H} , are derived for the ZUPT.

In general,

$$\hat{\mathbf{V}}_{\text{enu}} = \mathbf{V}_{\text{enu}} + \delta\hat{\mathbf{V}}_{\text{enu}} \quad (39)$$

where

$\hat{\mathbf{V}}_{\text{enu}}$ = the corrected velocities in ENU coordinates

\mathbf{V}_{enu} = the velocities calculated by INS

$\delta\hat{\mathbf{V}}_{\text{enu}}$ = the filter calculated velocities error value.

Using ZUPT,

$$\hat{\mathbf{V}}_{\text{enu}} \cdot \mathbf{n}_1 = (\mathbf{V}_{\text{enu}} + \delta\hat{\mathbf{V}}_{\text{enu}}) \cdot \mathbf{n}_{x,\text{enu}} = \mathbf{0} \quad (40)$$

where $\mathbf{n}_{x,\text{enu}}$ is the zero velocity vector ($x = 1, 2$).

Hence,

$$-\mathbf{V}_{\text{enu}} \cdot \mathbf{n}_{x,\text{enu}} = \delta\hat{\mathbf{V}}_{\text{enu}} \cdot \mathbf{n}_{x,\text{enu}} \quad (41)$$

where $-\mathbf{V}_{\text{enu}} \cdot \mathbf{n}_{x,\text{enu}}$ = the image measurement, $z_{\text{image}, x}$.

The measurement matrix $\mathbf{H}_{\text{image}}$ for the ZUPT is as shown

$$\mathbf{H}_{\text{image}} = \begin{bmatrix} n_{1e} & n_{1n} & n_{1u} \\ n_{2e} & n_{2n} & n_{2u} \end{bmatrix} \quad (42)$$

where

n_{1e}, n_{1n}, n_{1u} are the 1st null vector expressed in local level ENU coordinates
 n_{2e}, n_{2n}, n_{2u} are the 2nd null vector expressed in local level ENU coordinates.

3.3.4 GPS Measurement Model.

A tightly coupled method was used in this research to integrate GPS with INS. The GPS measurement is a pseudorange measurement from the receiver to each visible satellite. The INS also generates its own estimate of the same pseudorange. The difference between these two measurements are used to derive measurement(s) for the Kalman filter as shown in Eq (43). This method of integration allows GPS measurements to be used by the INS, even when there are less than four pseudorange measurements required by the GPS itself to determine the position. The derivation of the GPS measurement matrix, \mathbf{H}_{GPS} , is shown in Eq (43) to (47). Further details on the derivation can be found in (Noureldin et al., 2013).

$$\mathbf{z}_{GPS} = \boldsymbol{\rho}_{INS} - \boldsymbol{\rho}_{GPS} \quad (43)$$

For m visible satellites, Eq (43) can be expanded into Eq (44) and (45).

$$\mathbf{z}_{GPS} = \begin{bmatrix} \rho_{INS}^1 - \rho_{GPS}^1 \\ \vdots \\ \rho_{INS}^m - \rho_{GPS}^m \end{bmatrix} \quad (44)$$

$$\mathbf{z}_{GPS} = \begin{bmatrix} l_{x,INS}^1 & l_{y,INS}^1 & l_{z,INS}^1 \\ \vdots & \vdots & \vdots \\ l_{x,INS}^m & l_{y,INS}^m & l_{z,INS}^m \end{bmatrix}_{m \times 3} \begin{bmatrix} \delta x \\ \delta y \\ \delta z \end{bmatrix}_{3 \times 1} - c \begin{bmatrix} \delta b_r \\ \vdots \\ \delta b_r \end{bmatrix}_{m \times 1} \quad (45)$$

where

l_{INS}^m = the line of sight unit vector from the receiver to the m^{th} satellite in the receiver's ECEF frame.

$\delta x, \delta y, \delta z$ = the position error of the receiver in ECEF coordinates.

Eq (45) can be re-written in terms of geodetic coordinates as shown in Eq (46) and (47).

$$\mathbf{z}_{\text{GPS}} = \begin{bmatrix} l_{x,INS}^1 & l_{y,INS}^1 & l_{z,INS}^1 \\ \vdots & \vdots & \vdots \\ l_{x,INS}^m & l_{y,INS}^m & l_{z,INS}^m \end{bmatrix}_{m \times 3} \begin{bmatrix} -(R_N + h) \sin \varphi \cos \lambda & -(R_N + h) \cos \varphi \sin \lambda & \cos \varphi \cos \lambda \\ -(R_N + h) \sin \varphi \sin \lambda & (R_N + h) \cos \varphi \cos \lambda & \cos \varphi \sin \lambda \\ \{R_N(1 - e^2) + h\} \cos \varphi & 0 & \sin \varphi \end{bmatrix}_{3 \times 3} \begin{bmatrix} \delta \varphi \\ \delta \lambda \\ \delta h \end{bmatrix}_{3 \times 1} - c \begin{bmatrix} \delta b_r \\ \vdots \\ \delta b_r \end{bmatrix}_{m \times 1} \quad (46)$$

$$\mathbf{z}_{\text{GPS}} = \mathbf{H}_{\text{GPS}}_{m \times 3} \begin{bmatrix} \delta \varphi \\ \delta \lambda \\ \delta h \end{bmatrix}_{3 \times 1} - c \begin{bmatrix} \delta b_r \\ \vdots \\ \delta b_r \end{bmatrix}_{m \times 1} \quad (47)$$

3.3.5 Overall Measurement Model.

The measurement model for the image provided by Eq (42) and the measurement model for the pseudorange provided by Eq (47) can be combined to create an overall measurement model as shown

$$\begin{bmatrix} Z_{\text{image},1} \\ Z_{\text{image},2} \\ Z_{\text{GPS},1} \\ \vdots \\ Z_{\text{GPS},m} \end{bmatrix} = \begin{bmatrix} \mathbf{0}_{2 \times 3} & \mathbf{H}_{\text{image}}_{2 \times 3} & \mathbf{0}_{2 \times 9} & \mathbf{0}_{2 \times 1} & \mathbf{0}_{2 \times 1} \\ \mathbf{H}_{\text{GPS}}_{m \times 3} & \mathbf{0}_{m \times 3} & \mathbf{0}_{2 \times 9} & -c_{m \times 1} & \mathbf{0}_{m \times 1} \end{bmatrix} \begin{bmatrix} \mathbf{x}_{\text{INS}} \\ \mathbf{x}_{\text{GPS}} \end{bmatrix} \quad (48)$$

These measurements are incorporated into the navigation filter using the Kalman measurement update equations. The PVA error states after the measurement updates are used to correct errors in the VINS.

3.4 Verification of Simulation Platform

Using the VINS model described in the previous section, the data generated from the simulation platform was verified for its accuracy in two main phases. The first phase verified each component of the simulation platform individually while the second phase verified the simulation platform as a whole.

The IMU was verified by adding a small amount of noise to the simulated ΔV and $\Delta\theta$ measurements. Without including any measurement updates, positions calculated from the VINS model were then checked to ensure that they replicated the truth closely. The same approach was also used to verify the simulated GPS pseudoranges. To verify the simulated features, the direction of translation computed using the matched features were verified against the true direction of translation.

Verification of the whole simulation platform was performed by incorporating both GPS and image measurements with the IMU. The covariance of the error states and the error states were verified for the correct order of magnitude.

3.5 Summary

This chapter described the requirements for the simulation platform, and how it was designed, built and verified. An error model integrated with visual odometry and GPS pseudorange measurements was built to verify the accuracy of the data generated from the simulation platform.

IV. Analysis and Results

The utility of the simulation platform was demonstrated by making use of it to conduct a trade study on the design of a VINS. The results from this trade study are discussed in this chapter. A total of 36 test cases, each comprising a different set of design parameters for a VINS, were analyzed. The performance measures used to compare results among the different test cases were (1) the average Distance Root Mean Square (DRMS) errors along the trajectory, and (2) the percentage error of DRMS error over distance traveled.

4.1 Scenarios for Trade Study

The simulation platform was tested using 6 sets of real-world images and 3 sets of PVA data collected from a ground vehicle as part of the ASPN program. The ASPN program identified the 3 sets of PVA data as ‘Scenario 2’, ‘Scenario 6’ and ‘Scenario 7’. To ensure consistency with the ASPN program, the same names were adopted for this research. 2 sets of photos, from a side-looking camera and a forward-looking camera, were collected from each scenario.

4.1.1 Scenario 2.

Scenario 2 depicted driving a vehicle around an urban environment in daylight with numerous low-rise buildings along the way. The distance travelled was 2463.5m and the duration was 420 seconds. The horizontal trajectory is shown in Figure 16. The altitude of the vehicle ranges from 159.5m to 165.3m as shown in Figure 17. The number of matched features, found using SIFT and epipolar constraints from the side and front camera, is shown in Figure 18 and Figure 19 respectively.

4.1.2 Scenario 6.

Scenario 6 depicted driving a vehicle in rectangular circuits around a carpark lot during the day. The heading angle of the vehicle changes rapidly compared to the other scenarios. The distance travelled was 1664.2m and the duration was 325 seconds. The trajectory is shown in Figure 20 and the altitude of the vehicle ranges from 190.0m to 191.8m as shown in Figure 21. The number of matched features, found using SIFT and epipolar constraints from the side and front camera, is shown in Figure 22 and Figure 23 respectively.

4.1.3 Scenario 7.

Scenario 7 is a scenario of driving a vehicle around a city area with high rise buildings and multiple traffic stops during the day. The distance travelled was 3012.0m and the duration was 600 seconds. The trajectory is shown in Figure 24 and the altitude of the vehicle ranges from 194.0m to 202.1m as shown in Figure 25. The number of matched features, found using SIFT and epipolar constraints from the side and front camera, is shown in Figure 26 and Figure 27 respectively.

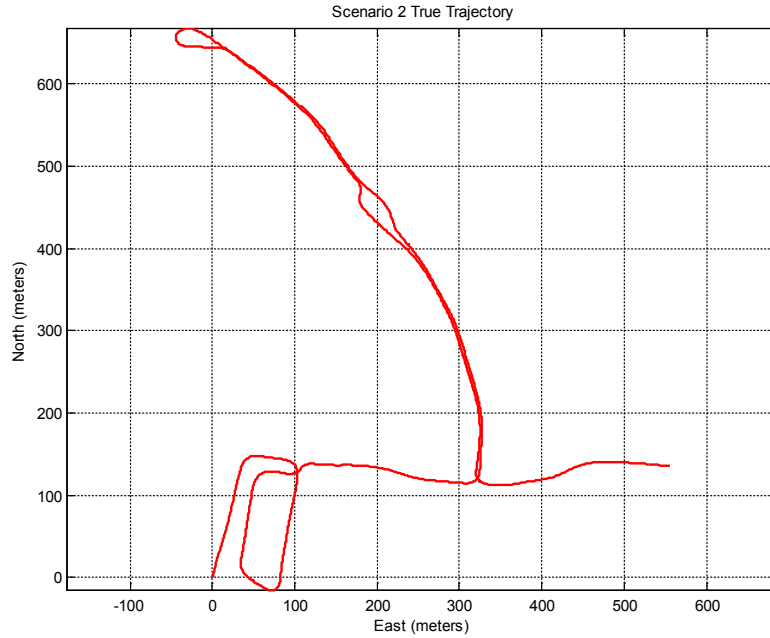


Figure 16. True Horizontal Trajectory (Scenario 2). All the horizontal trajectory plots in this thesis starts at (0, 0). The turns in this scenario were smoother compared to the turns in Scenario 7.

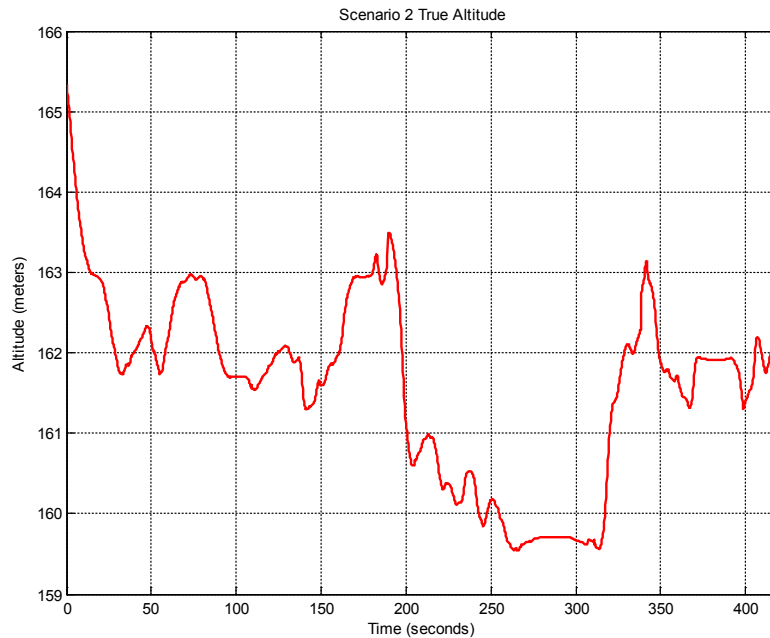


Figure 17. True Altitude (Scenario 2). As these scenarios were recorded using a ground vehicle, the change in altitude are minimal compared to an aerial vehicle.

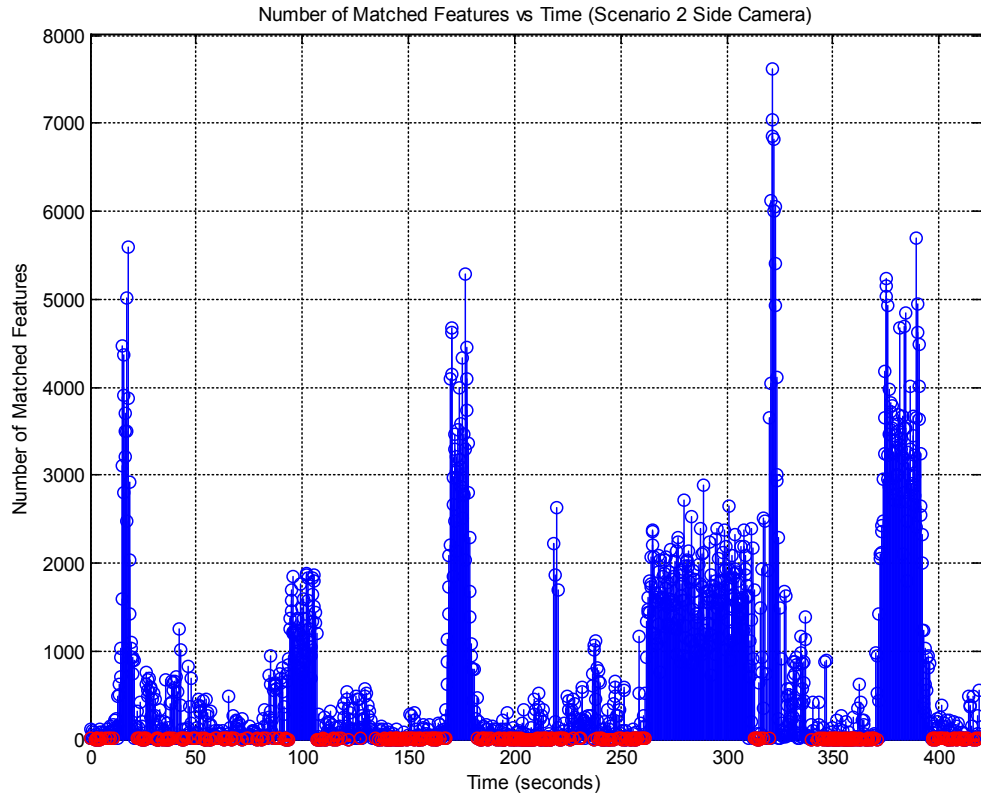


Figure 18. Number of Matched Features Found from Scenario 2 Side Camera Images. There are a total of 1677 pairs of images in this scenario. The blue lines indicate 1301 time instances where there are more than 3 matched features, and hence updates to the navigation solution from image measurements. The red circles indicate 376 time instances where there are less 3 matched features, and hence no update to the navigation solution from image measurement.

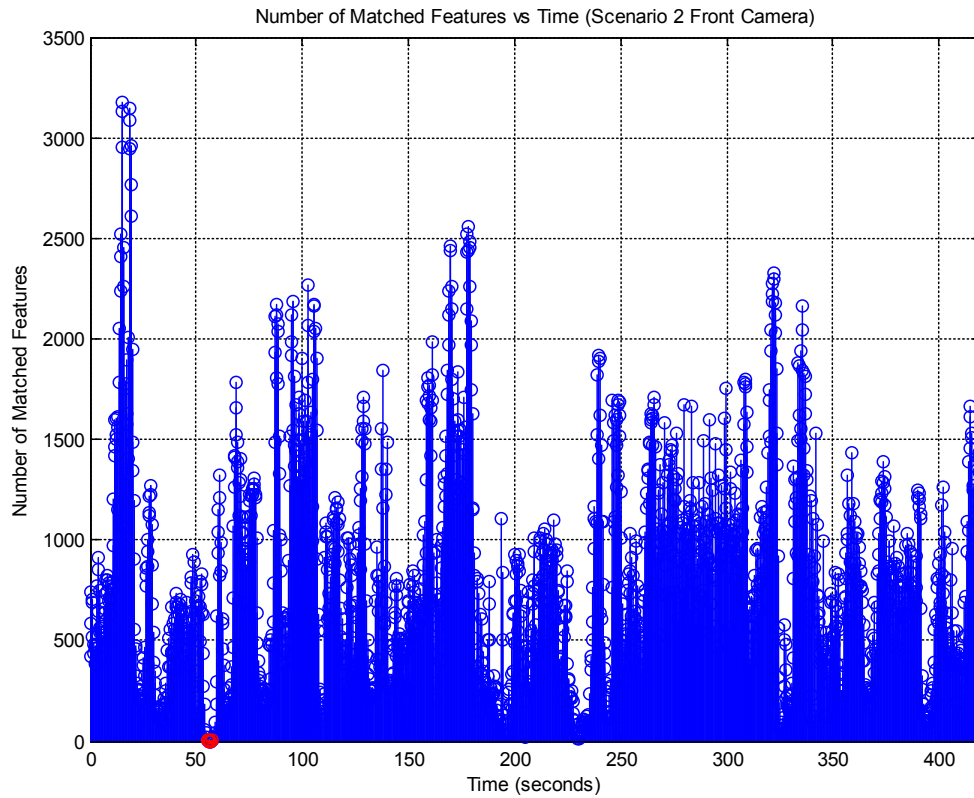


Figure 19. Number of Matched Features Found from Scenario 2 Front Camera Images. There are a total of 1677 pairs of images in this scenario. The blue lines indicate 1670 time instances where there are more than 3 matched features, and updates to the navigation solution from image measurements. The red circles indicate 7 time instances where there are less 3 matched features, and no update to the navigation solution from image measurement. These were due to damaged images as the camera faced direct glare from sunlight

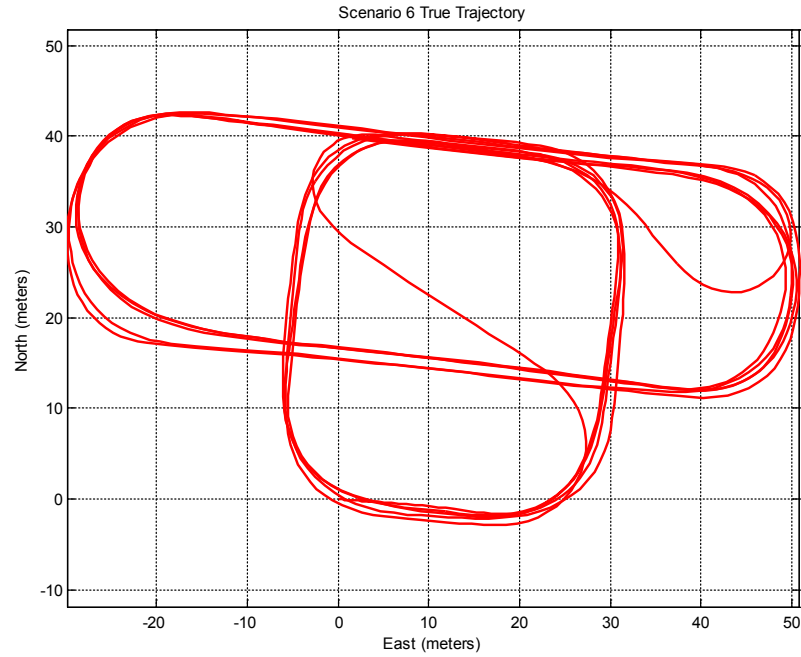


Figure 20. True Horizontal Trajectory (Scenario 6). While the distance travelled in this scenario was around 1664m, the maximum displacement was smaller (50m) compared to the other scenario.

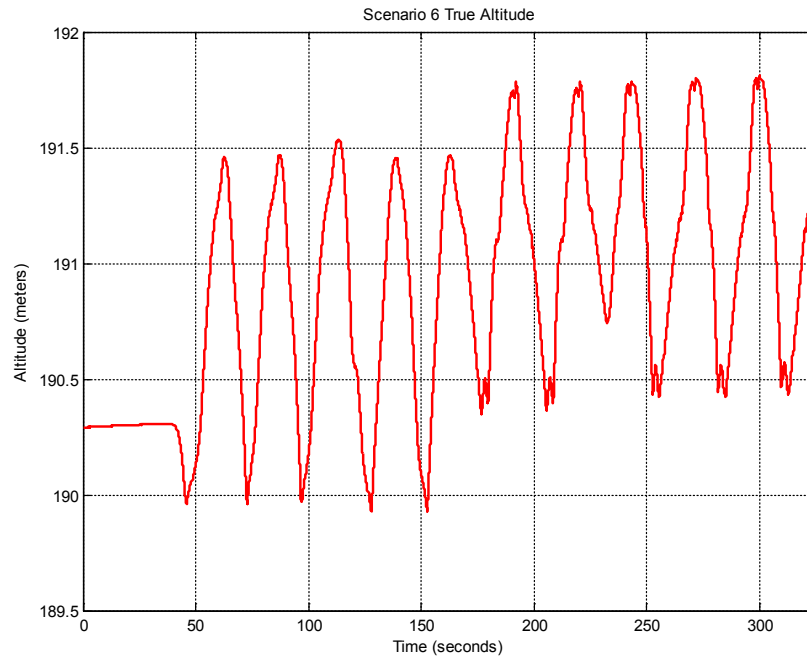


Figure 21. True Altitude (Scenario 6). Among the 3 scenarios, this scenario had the least variation in altitude.

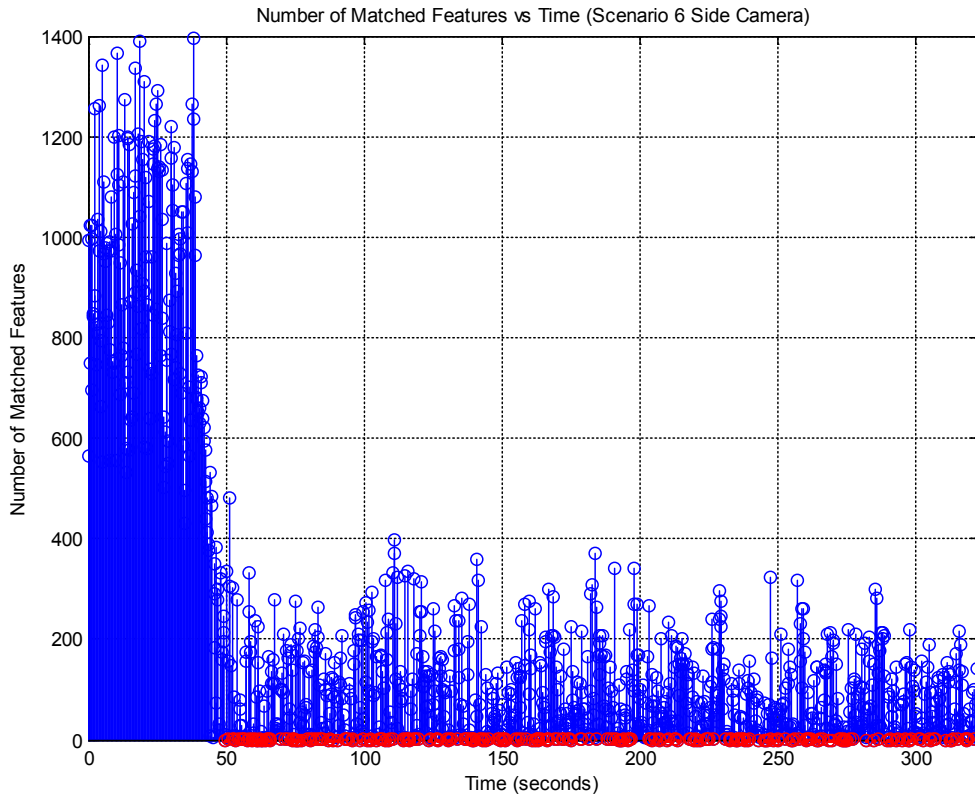


Figure 22. Number of Matched Features Found from Scenario 6 Side Camera Images. There are a total of 1290 pairs of images in this scenario. The blue lines indicate 1018 time instances where there are more than 3 matched features, and updates to the navigation solution from image measurements. The red circles indicate 272 time instances where there are less 3 matched features, and no update to the navigation solution from image measurement. There are a high number of matched features in the first 50 seconds as the vehicle was stationary during this period of time.

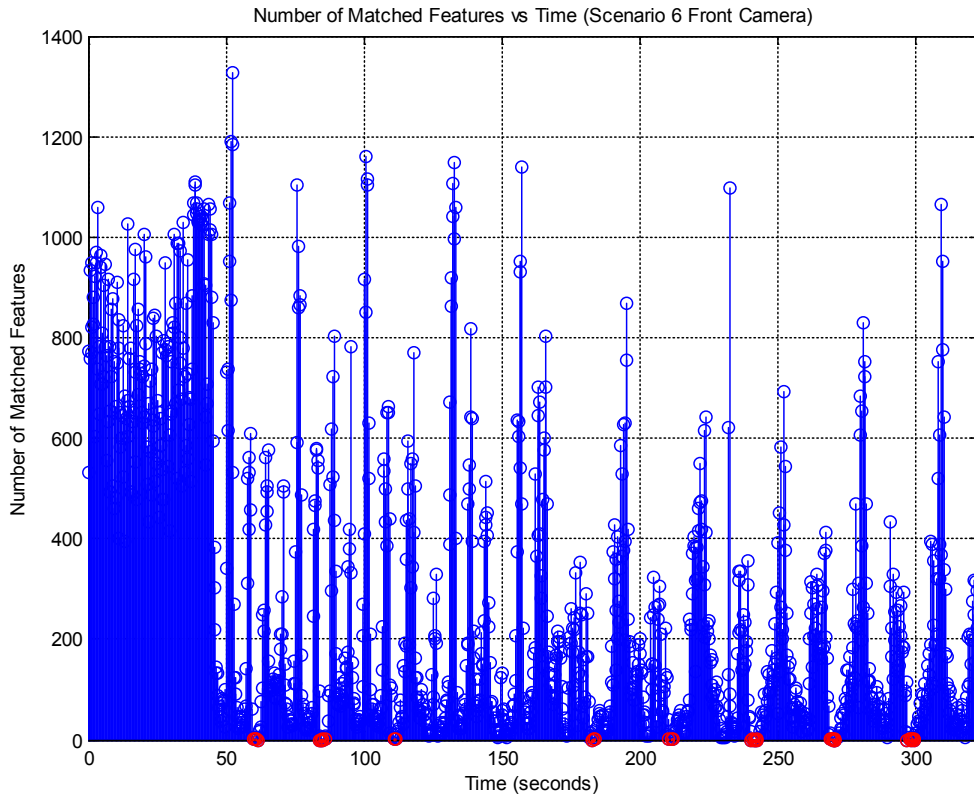


Figure 23. Number of Matched Features Found from Scenario 6 Front Camera Images. There are a total of 1290 pairs of images in this scenario. The blue lines indicate 1241 time instances where there are more than 3 matched features, and updates to the navigation solution from image measurements. The red circle indicates 49 time instances where there are less 3 matched features, and no update to the navigation solution from image measurement. These happened when the vehicle was making rapid heading changes.

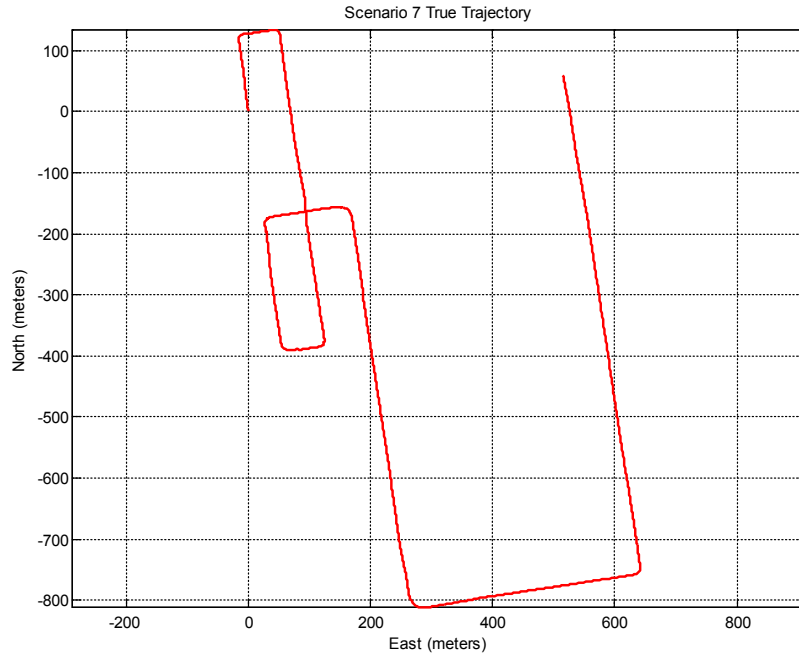


Figure 24. True Horizontal Trajectory (Figure 7). This scenario depicted driving in a city area where there were many right angle turns, with constant headings in between turns.

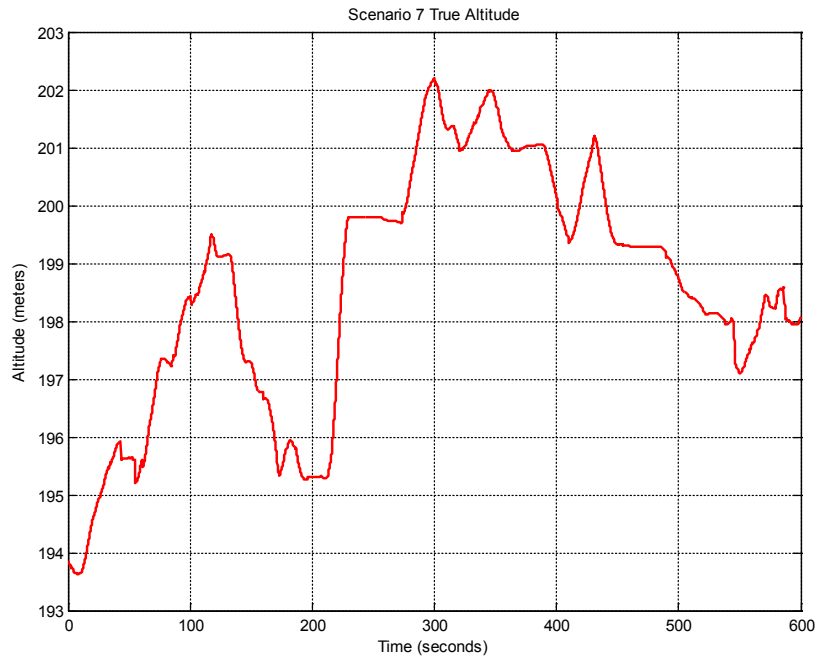


Figure 25. True Altitude (Scenario 7). This scenario has the largest change in altitude among the 3 scenarios.

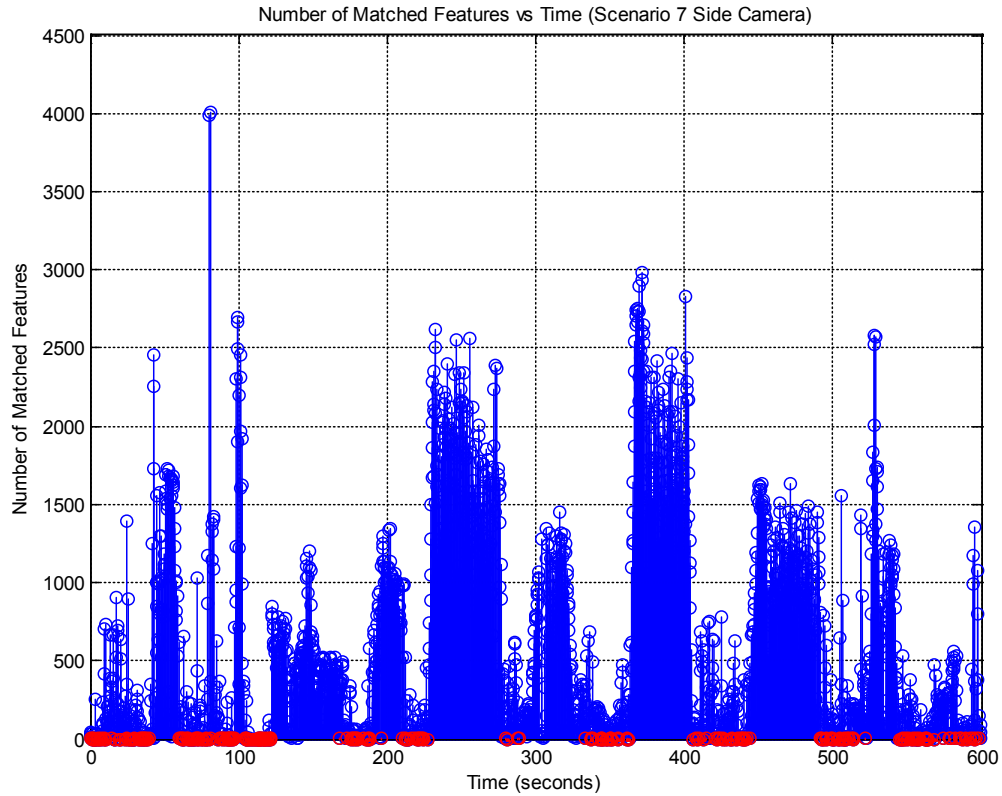


Figure 26. Number of Matched Features Found from Scenario 7 Side Camera Images. There are a total of 2399 pairs of images in this scenario. The blue lines indicate 2039 time instances where there are more than 3 matched features, and updates to the navigation solution from image measurements. The red circle indicate 360 time instances where there are less than 3 matched features, and no update to the navigation solution from image measurement. The reasons for having less than 3 matched features are attributed to either (1) damaged images as the camera faces direct glare from sunlight, (2) over exposed images as camera emerges from a dark location (e.g. underpass) to a brightly lit location, (3) dark images as the camera looks at a sheltered and unlit parking garage, etc.

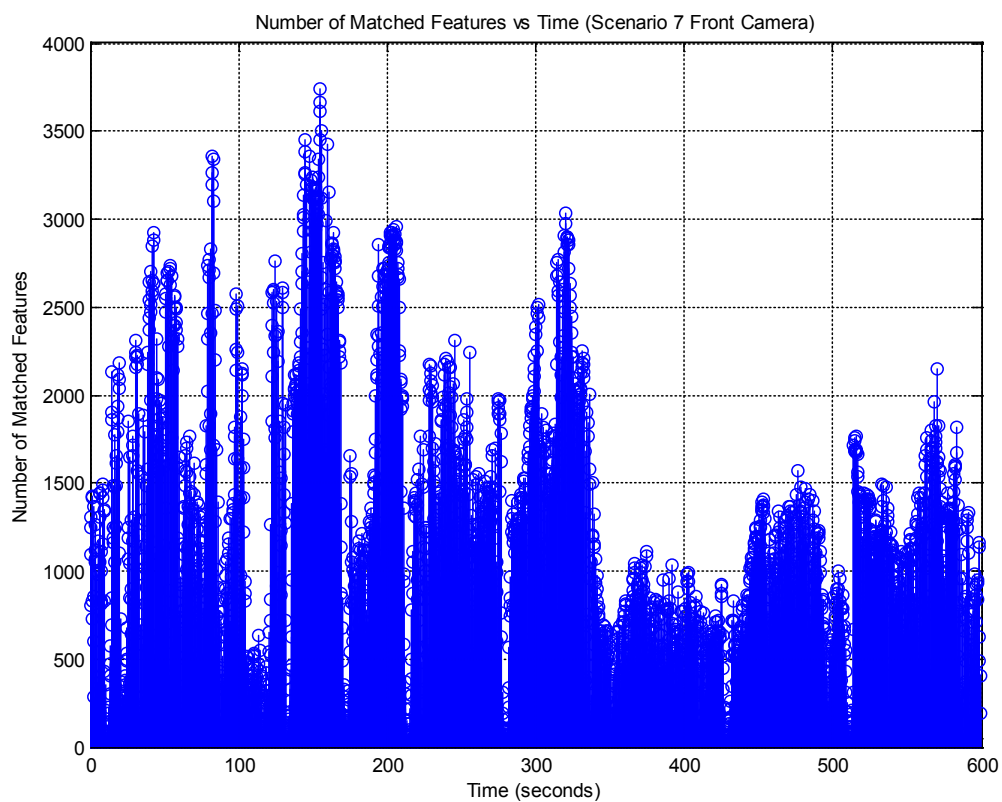


Figure 27. Number of Matched Features Found from Scenario 7 Front Camera Images. There are at least 42 matched features between all the 2399 successive pairs of images. This is the only set of photos where there are measurements from all the images.

4.2 Results from Trade Study

The trade study examined the effects of 7 parameters, as shown in Table 4, on the performance of a VINS. A total of 36 test cases, each comprising a different set of design parameters as shown in Table 5, were analyzed. The nominal test case was Scenario 2 Side Camera with a camera quality of 2 pixel noise, commercial grade IMU and crystal GPS receiver clock with 2 pseudorange measurements. 20 Monte Carlo runs of each test case were carried out. To ensure fair comparison among the test cases and replicability of results, the random number generator was reset at the beginning of each of the 20 runs. For each run, the following performances were calculated: (1) root mean square of the horizontal distance error (Distance Root Mean Square, DRMS) between the calculated position and the true position as shown in Eq (49), and (2) percentage of the DRMS error over the total distance travelled. The mean DRMS error over the 20 runs was then calculated as the final performance measure for each test case.

$$\text{DRMS} = \sqrt{\frac{\sum_{i=1}^n (x_i^2 + y_i^2)}{n}} \quad (49)$$

where n = the number of measurement epochs in the scenario

x_i, y_i = errors in the north and east direction for the i^{th} measurement.

Table 4. Parameters Examined in Trade Study

	Parameters	Options
1	Interval Between Updates	0.25 sec vs 1 sec
2	IMU Quality	Commercial, Tactical, Navigation
3	Camera Quality	Standard Deviation of Pixel Noise (0, 1, 2, 4, and 10)
4	Camera Pointing Direction	Front vs Side
5	Method of Zero Velocity Update	a. Calculate zero velocity vector using rotation from INS ('Cal t known R') b. Calculate zero velocity vector using rotation and translation from image measurements ('Cal t and R')
6	GPS Clock	Crystal, Ovenised Crystal, Rubidium
7	Number of Pseudorange Measurements	0 - 3

Table 5. Configurations of Test Cases. Changes to the nominal test case are highlighted in yellow.

Case Number	Image	Scenario	Update Interval (sec)	IMU	Pixel Noise	Camera	Translation	Clock	Number of Pseudorange Measurements
1 (Nominal)	Yes	2	0.25	Commercial	2	Side	Cal t known R	Crystal	2
2 (No Measurement)	No	2	NA	Commercial	NA	NA	NA	NA	0
3 (Full GPS View)	No	2	0.25	Commercial	NA	NA	NA	Crystal	12
4 (2 PR Case)	No	2	0.25	Commercial	NA	NA	NA	Crystal	2
5 (Image Only)	Yes	2	0.25	Commercial	2	Side	Cal t known R	NA	0

Interval Between Updates

1	Yes	2	0.25	Commercial	2	Side	Cal t known R	Crystal	2
6	Yes	2	1	Commercial	2	Side	Cal t known R	Crystal	2
7	Yes	6	0.25	Commercial	2	Side	Cal t known R	Crystal	2
8	Yes	6	1	Commercial	2	Side	Cal t known R	Crystal	2
9	Yes	7	0.25	Commercial	2	Side	Cal t known R	Crystal	2
10	Yes	7	1	Commercial	2	Side	Cal t known R	Crystal	2

IMU Quality

1	Yes	2	0.25	Commercial	2	Side	Cal t known R	Crystal	2
11	Yes	2	0.25	Tactical	2	Side	Cal t known R	Crystal	2
12	Yes	2	0.25	Navigation	2	Side	Cal t known R	Crystal	2
13	No	2	NA	Tactical	NA	NA	NA	NA	0
14	No	2	NA	Navigation	NA	NA	NA	NA	0

Camera Quality

1	Yes	2	0.25	Commercial	2	Side	Cal t known R	Crystal	2
15	Yes	2	0.25	Commercial	0	Side	Cal t known R	Crystal	2
16	Yes	2	0.25	Commercial	1	Side	Cal t known R	Crystal	2
17	Yes	2	0.25	Commercial	4	Side	Cal t known R	Crystal	2
18	Yes	2	0.25	Commercial	10	Side	Cal t known R	Crystal	2

Camera Pointing Direction

1	Yes	2	0.25	Commercial	2	Side	Cal t known R	Crystal	2
19	Yes	2	0.25	Commercial	2	Front	Cal t known R	Crystal	2
7	Yes	6	0.25	Commercial	2	Side	Cal t known R	Crystal	2
20	Yes	6	0.25	Commercial	2	Front	Cal t known R	Crystal	2
9	Yes	7	0.25	Commercial	2	Side	Cal t known R	Crystal	2
21	Yes	7	0.25	Commercial	2	Front	Cal t known R	Crystal	2

Method of Calculating Direction of Translation

1	Yes	2	0.25	Commercial	2	Side	Cal t known R	Crystal	2
22	Yes	2	0.25	Commercial	2	Side	Cal t and R	Crystal	2
7	Yes	6	0.25	Commercial	2	Side	Cal t known R	Crystal	2
23	Yes	6	0.25	Commercial	2	Side	Cal t and R	Crystal	2
9	Yes	7	0.25	Commercial	2	Side	Cal t known R	Crystal	2
24	Yes	7	0.25	Commercial	2	Side	Cal t and R	Crystal	2

GPS Clock

1	Yes	2	0.25	Commercial	2	Side	Cal t known R	Crystal	2
25	Yes	2	0.25	Commercial	2	Side	Cal t known R	Ovenised Crystal	2
26	Yes	2	0.25	Commercial	2	Side	Cal t known R	Rubidium	2
4	No	2	0.25	Commercial	NA	NA	NA	Crystal	2
27	No	2	0.25	Commercial	NA	NA	NA	Ovenised Crystal	2
28	No	2	0.25	Commercial	NA	NA	NA	Rubidium	2

Number of Pseudorange Measurements

1	Yes	2	0.25	Commercial	2	Side	Cal t known R	Crystal	2
29	Yes	2	0.25	Commercial	2	Side	Cal t known R	Crystal	1
30	Yes	2	0.25	Commercial	2	Side	Cal t known R	Crystal	3
31	Yes	2	0.25	Commercial	2	Side	Cal t known R	Crystal	4
32	Yes	2	0.25	Commercial	2	Side	Cal t known R	Crystal	8
4	No	2	0.25	Commercial	NA	NA	NA	Crystal	2
33	No	2	0.25	Commercial	NA	NA	NA	Crystal	1
34	No	2	0.25	Commercial	NA	NA	NA	Crystal	3
35	No	2	0.25	Commercial	NA	NA	NA	Crystal	4
36	No	2	0.25	Commercial	NA	NA	NA	Crystal	8

4.2.1 Accuracy of a Nominal VINS.

Table 6 lists the performance among a commercial INS without measurement updates, a commercial INS with 2 GPS pseudoranges, a commercial INS with image measurements, the nominal VINS configuration, and a commercial INS with full GPS view (12 pseudoranges). The results show the benefits of the nominal VINS, i.e. an INS that incorporates visual odometry and GPS pseudoranges while in a GPS limited environment. The nominal VINS had a position accuracy that was 2.5 times better than an INS that incorporate visual odometry only. Its position accuracy was 250 times better than an INS that incorporates 2 GPS pseudoranges. Figure 28 and Figure 29 shows the position errors and velocity errors of the nominal VINS configuration respectively. These results served as the motivation behind the trade study on the design of a VINS. While the position accuracy of the nominal VINS was approximately 59 times worse than an INS with full GPS view, the trade study would help to identify key parameters that could be changed to improve its performance.

Table 6. Accuracy of a nominal VINS. Comparison of performance to the nominal test case in this thesis is calculated by taking the ratio of the DRMS error in nominal case to the DRMS error in the test case. A ratio that is more than 1 indicates a better performance for the test case while a ratio that is less than 1 indicates a worse performance for the test case.

Description of Test Case	DRMS (m)	DRMS / Distance Travelled (%)	Performance Compared to Nominal
No Measurement	24915.0	1011.4	0.003
2 Pseudoranges with no Image	20969.0	851.2	0.004
Image Only	183.8	7.5	0.4
2 Pseudoranges with Image (Nominal)	77.0	3.1	1.0
Full GPS View	1.3	0.05	59.2

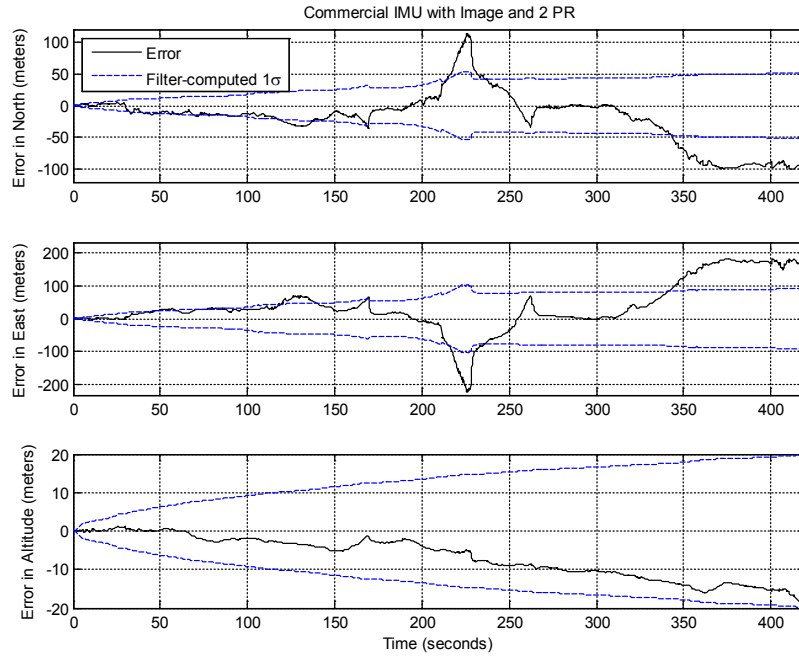


Figure 28. Position Errors of Nominal VINS Configuration. In this thesis, the blue dotted lines indicate the standard deviation of the error computed by the filter, while the black line shows the error from a single simulation run.

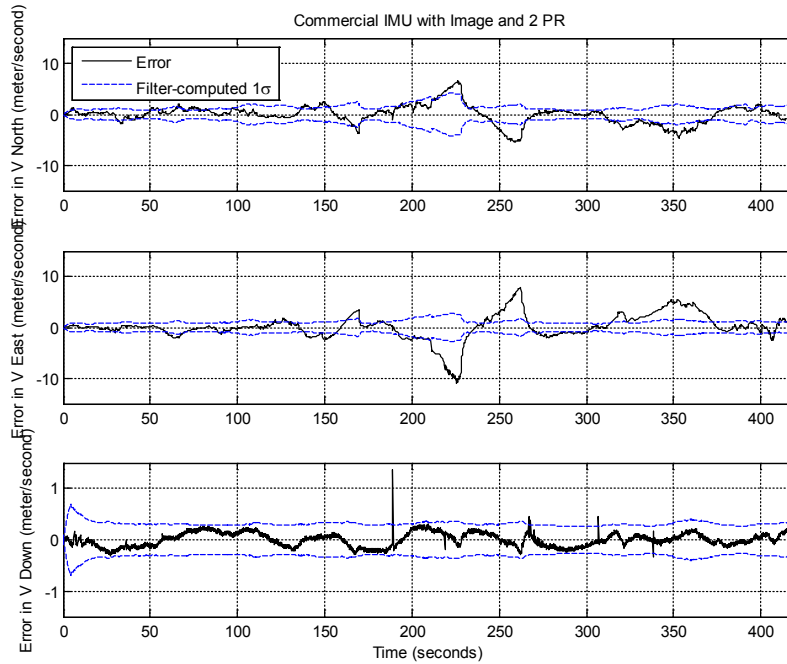


Figure 29. Velocity Errors of Nominal VINS Configuration

4.2.2 Interval between Update.

A key design parameter for a VINS is the interval between update. A shorter update interval would require the VINS to have a higher real-time computation requirement and also a camera capable of taking images at the required update interval. Table 7 compared the effects of varying the update interval from 0.25 sec to 1 sec for all three scenarios. The results showed that a longer update interval had a negative effect on the position accuracy. It would increase the DRMS error by 1.6 times to 31.5 times.

Scenario 6 had the highest increase in DRMS error as the vehicle in this scenario had a higher rate heading changes. Therefore, the update interval of 1 second was too slow to capture the motion of the vehicle accurately. In comparison, Scenarios 2 and 7 had slower rate heading changes. Hence, an update interval of 1 second had less detrimental effect on the position accuracy of the system.

Table 7. Effects of Interval between Updates on Accuracy of Position. The performance of 0.25 sec update interval is compared to 1 sec update interval. A value that is more than 1 indicates a better performance for a 0.25 sec update interval while a value that is less than 1 indicates a worse performance for a 0.25 sec update interval.

Scenario	DRMS - 0.25 sec Update Interval (m)	DRMS - 1 sec Update Interval (m)	Performance of 0.25 sec Update Interval Compared to 1 sec Update Interval
2	77.0	126.7	1.6
6	43.7	1378.0	31.5
7	80.3	231.4	2.9

4.2.3 IMU Quality.

The performance of a VINS is directly related to the IMU quality. This was validated by the results shown in Table 8. While a low-cost VINS is most likely to use a commercial grade INS, the trade study considered the improvement in position accuracy if a tactical grade or a navigation grade IMU was used. The tactical grade IMU performed approximate 1.9 times better than a commercial grade IMU, while a navigation grade IMU performed approximately 36.7 times better. Table 9 shows the effects of incorporating image measurements into the 3 different grades of IMU. By incorporating image measurements, there are improvements in the position accuracy for all 3 grades of IMU. The comparisons between the trajectories, position errors and velocity errors are shown in Figure 30 to Figure 34.

Table 8. Effects of Grade of IMU on Accuracy of Position

IMU Grade	DRMS (m)	DRMS / Distance Travelled (%)	Performance Compared to Nominal
Commercial (nominal)	77.0	3.1	1
Tactical	41.5	1.7	1.9
Navigation	2.1	0.08	36.7

Table 9. Effects of Grade of IMU on Accuracy of Position (with Image Measurements and without Image Measurements). The performance of IMU with image measurements is compared to IMU without image measurement. A value that is more than 1 indicates a better performance for an IMU with image measurement while a value that is less than 1 indicates a worse performance for an IMU with image measurement.

IMU Grade	DRMS – with Image (m)	DRMS - without Image (m)	Performance of IMU with Image Measurement Compared to IMU without Image Measurement
Commercial (nominal)	77.0	24915.0	323.6
Tactical	41.5	319.6	7.7
Navigation	2.1	2.2	1.05

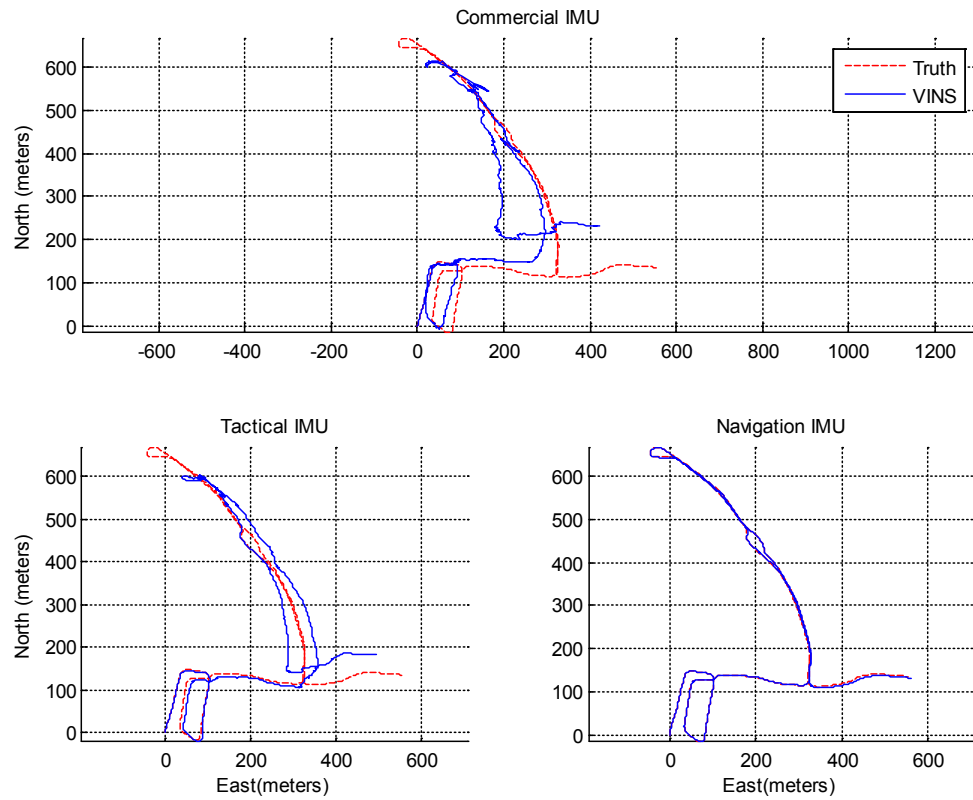


Figure 30. Comparison of Trajectories among Different Grades of IMU. The red dotted lines show the true trajectories while the blue lines show the computed trajectory from the VINS.

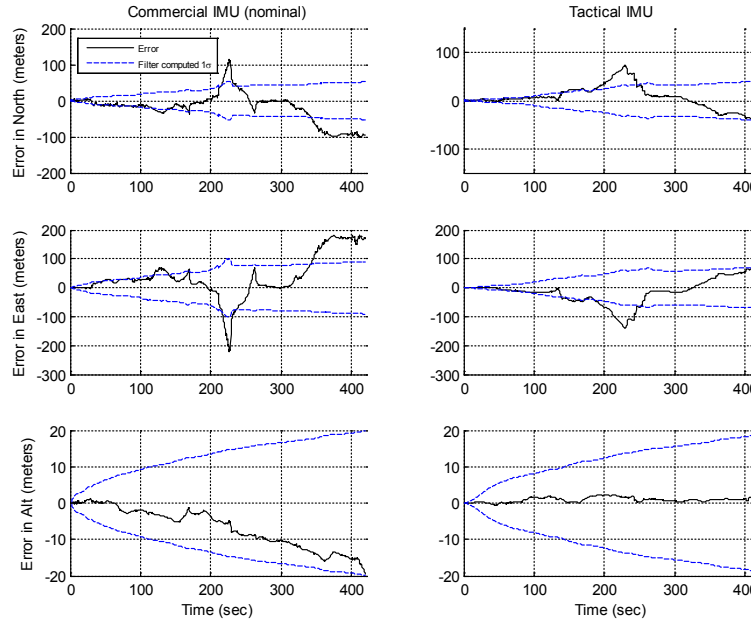


Figure 31. Comparison of Position Error (Commercial IMU vs Tactical IMU). For the comparison of position and velocity errors in this thesis, the blue dotted lines indicate the standard deviation of the error while the black line shows the results from a single simulation run.

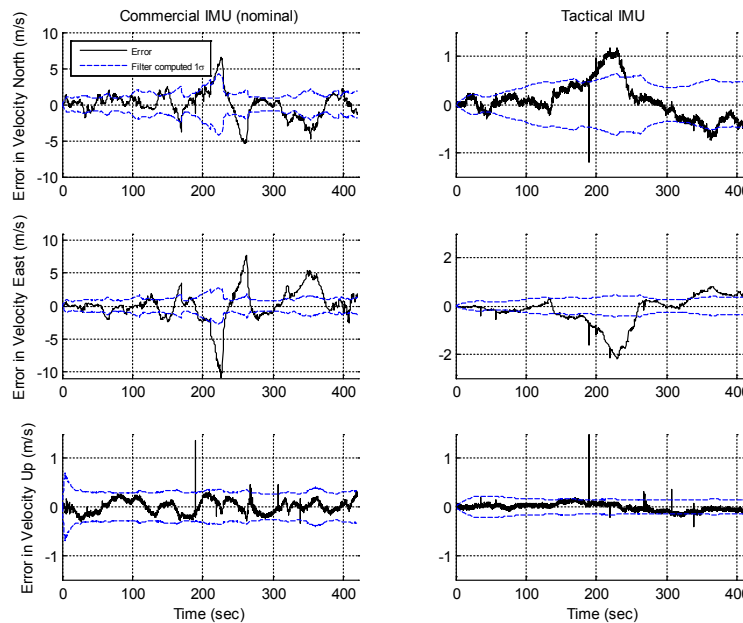


Figure 32. Comparison of Velocity Error (Commercial IMU vs Tactical IMU). The magnitude of velocity errors from the tactical IMU are smaller compared to the commercial IMU.

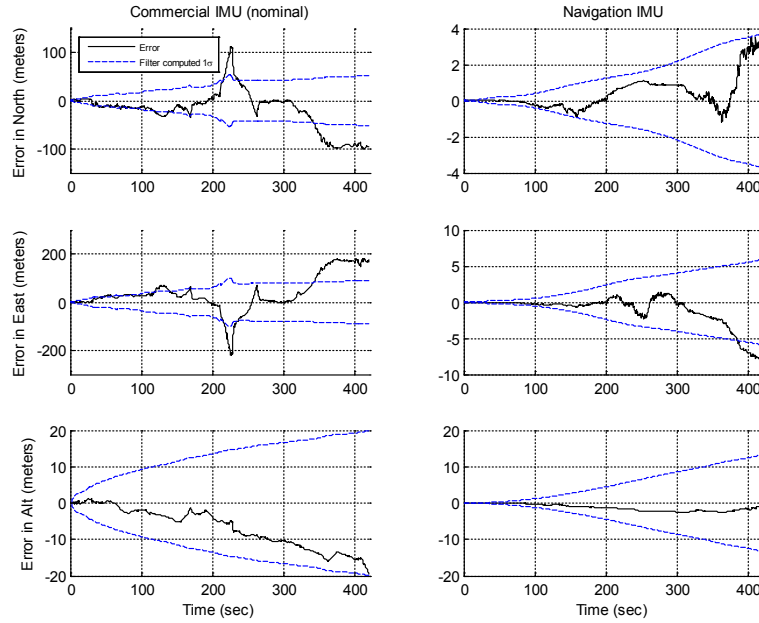


Figure 33. Comparison of Position Error (Commercial IMU vs Navigation IMU). The commercial IMU has horizontal position errors that are in the order of hundreds of meters, whereas the navigation IMU has horizontal position error in the order of meters.

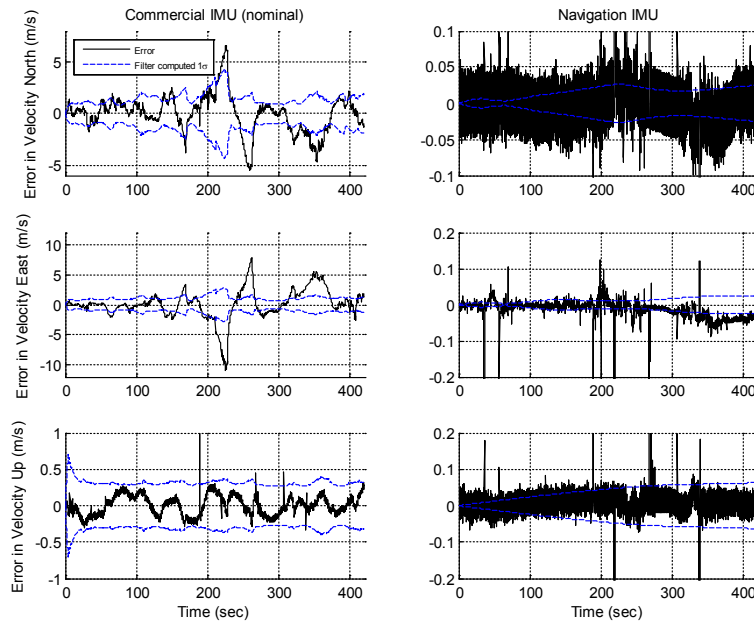


Figure 34. Comparison of Velocity Error (Commercial IMU vs Navigation IMU). The velocity errors for a navigation IMU are close to zero whereas the commercial IMU has errors that range from -5 to 5 m/s for velocity in the North direction and -10 to 10 m/s for velocity in the East direction.

4.2.4 Quality of Camera.

The quality of camera is a key design parameter of a VINS. In this thesis, this quality was characterized by inaccuracy associated with the pixel coordinates of features on images taken by the camera. Table 10 shows the performance of the VINS as the quality of the camera was varied from 0 pixel to 10 pixels. As the camera quality was improved from 2 pixels (nominal) to 0 pixel, there was an approximate 33% improvement in the position accuracy. Similarly, as the camera quality was worsened from 2 pixels to 4 pixels, there was an approximate 34% drop in the position accuracy. The position accuracy worsen by approximately 66% when the camera quality was worsen from 2 pixel to 10 pixel.

Table 10. Effects of Quality of Camera on Accuracy of Position

Standard Deviation of Noise in Image (pixel)	Standard Deviation of Measurement Noise (Vector 1)	Standard Deviation of Measurement Noise (Vector 2)	DRMS (m)	DRMS / Distance Travelled (%)	Performance Compared to Nominal
0	0.8239	0.2120	58.1	2.4	1.33
1	0.9532	0.2048	66.1	2.7	1.16
2 (nominal)	1.1881	0.2167	77.0	3.1	1
4	1.9368	0.2867	115.4	4.7	0.67
10	3.9470	0.4693	228.8	9.3	0.34

As noise associated with image measurement was not known prior to this thesis, the simulation platform was also used to determine this noise level. It was calculated by computing the differences between true ZUPT measurements and computed ZUPT measurements. The results are shown in Figure 35. It was observed that the noise measurement for the 2nd null vector was always smaller than that of the 1st vector. As the 2nd null vector in the simulation platform was typically in the vertical direction and the 1st

null vector was typically in the cross-track direction, it was postulated that the smaller velocity errors in the upwards direction led to a smaller noise measurement for the 2nd null vector.

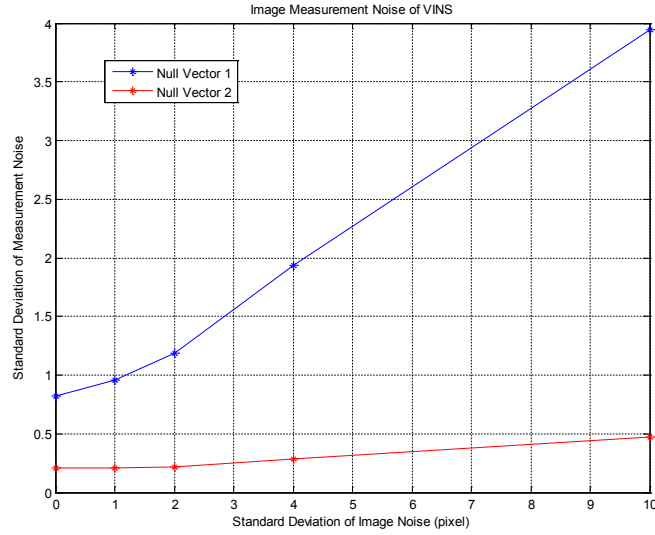


Figure 35. Image Measurement Noise of VINS

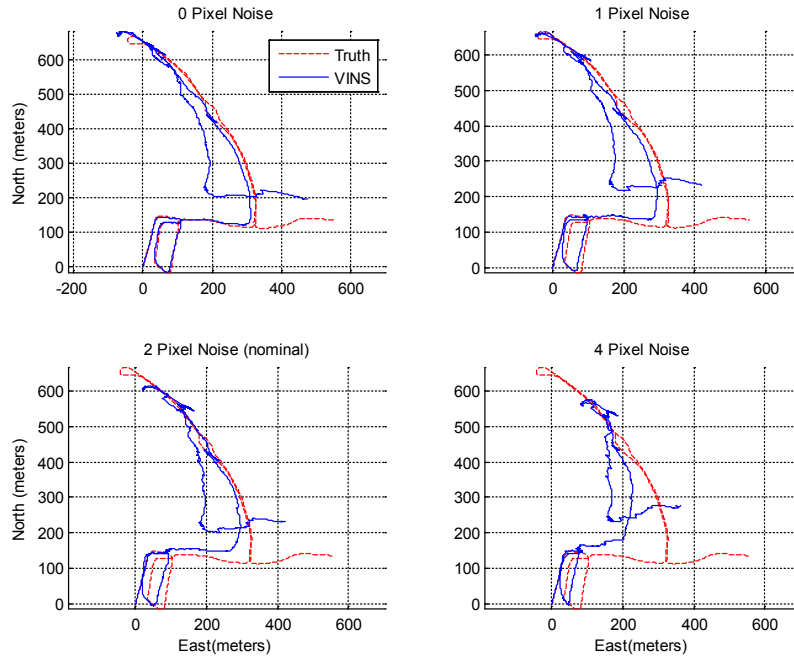


Figure 36. Comparison of Trajectories among Different Camera Quality. The trajectory with 4 pixel noise is considerably worse compared to the trajectory with 0 pixel noise.

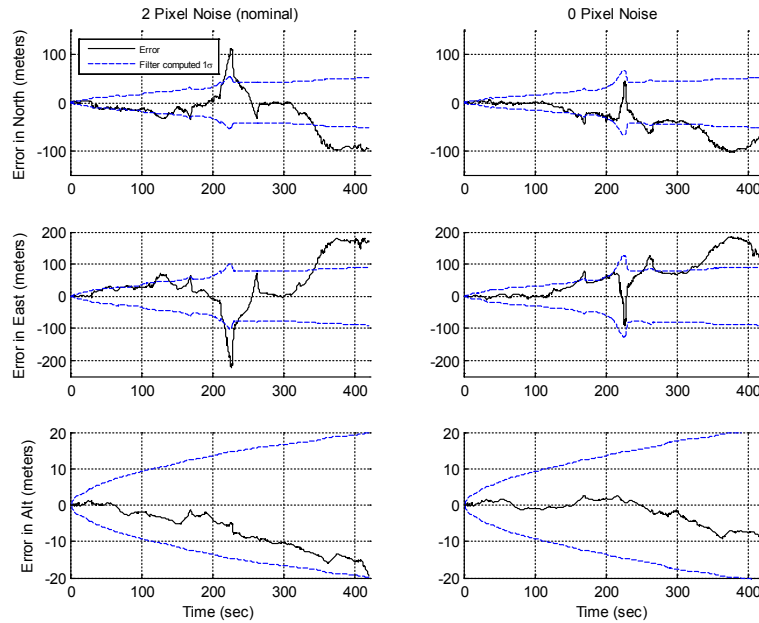


Figure 37. Comparison of Position Error (2 Pixel Noise vs 0 Pixel Noise). Position errors with 0 pixel noise are smaller compared to position error with 2 pixel noise.

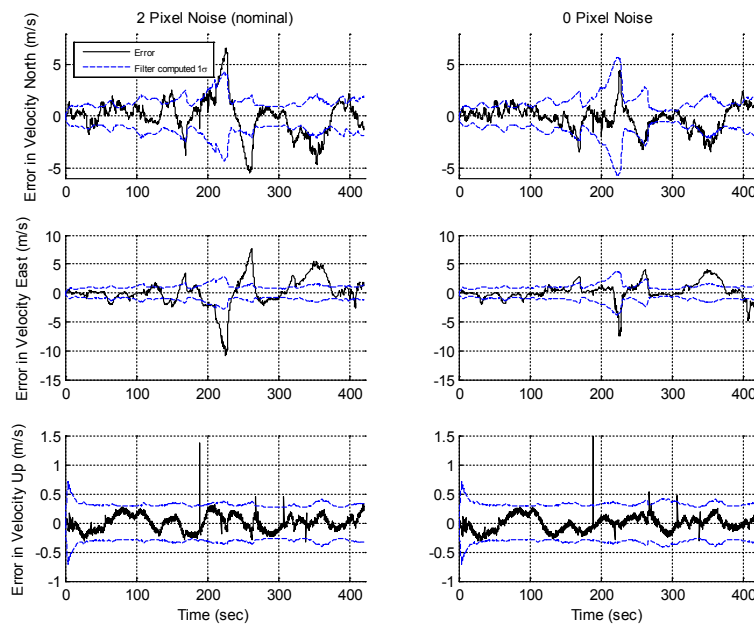


Figure 38. Comparison of Velocity Error (2 Pixel Noise vs 0 Pixel Noise). Velocity errors with 0 pixel noise are similar to velocity error with 2 pixel noise. Velocity errors in the Up direction are smaller compared to the East and North direction.

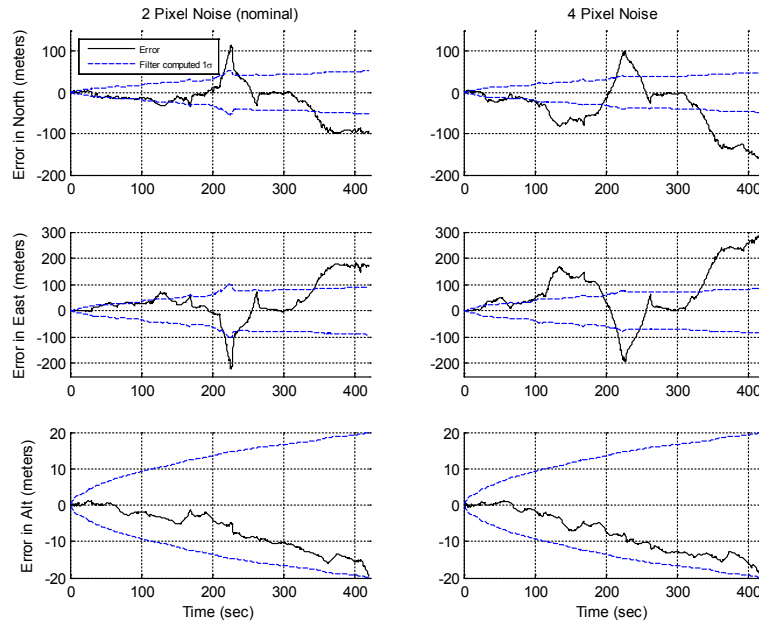


Figure 39. Comparison of Position Error (2 Pixel Noise vs 4 Pixel Noise). Position errors with 4 pixel noise are slightly larger compared to 2 pixel noise.

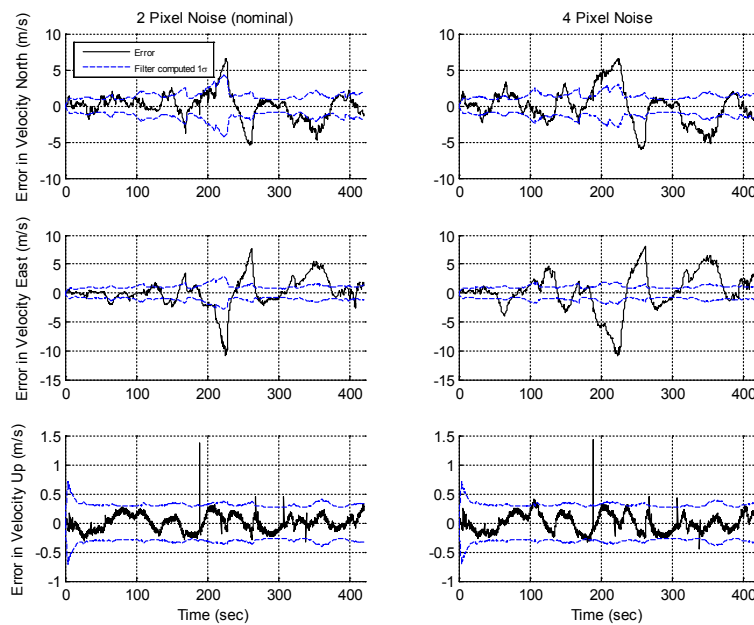


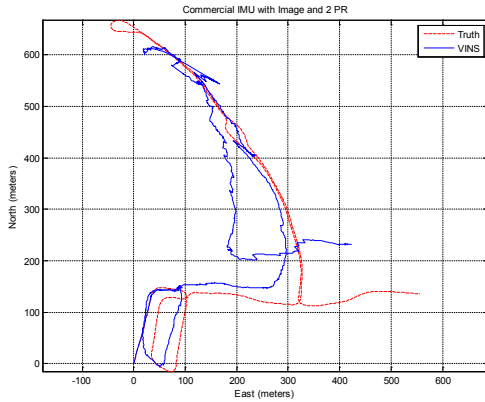
Figure 40. Comparison of Velocity Error (2 Pixel Noise vs 4 Pixel Noise). Magnitude of velocity errors are similar with 2 pixel noise and 4 pixel noise.

4.2.5 Camera Pointing Direction.

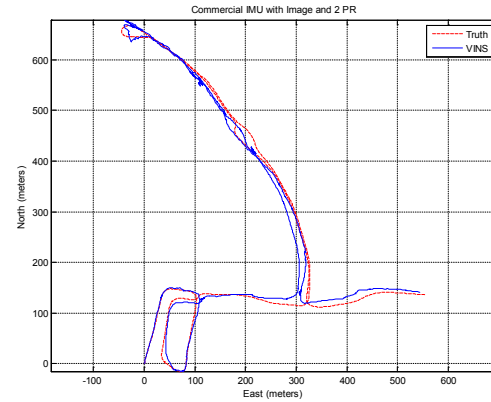
The figures in Section 4.2 showed that the pointing direction of a camera had an effect on the number of features that could be matched. The effect of a camera pointing direction on the position accuracy of a VINS was not evident prior to this thesis. Hence, the simulation platform was used to study this relationship and the results are presented in Table 11. For all 3 scenarios, there was a marginal improvement in a forward-looking camera compared to a side-looking camera. This could be attributed to the observation that images from a forward-looking camera produced more matched features compared to images from a side-looking camera. Figure 41, Figure 42 and Figure 43 show the comparison between the side and forward-looking cameras for Scenario 2, 6, and 7 respectively.

Table 11. Effects of Camera Pointing Direction on Accuracy of Position. The performance of integrating images from a forward looking camera is compared to the performance of integrating images from a side looking camera. A value that is more than 1 indicates a better performance for a forward looking camera while a value that is less than 1 indicates a worse performance.

Scenario	DRMS – Side Looking (m)	DRMS – Forward Looking (m)	Performance of Forward Looking Camera Compared to Side Looking Camera
2	77.0	76.0	1.01
6	43.7	36.6	1.19
7	80.3	74.8	1.07

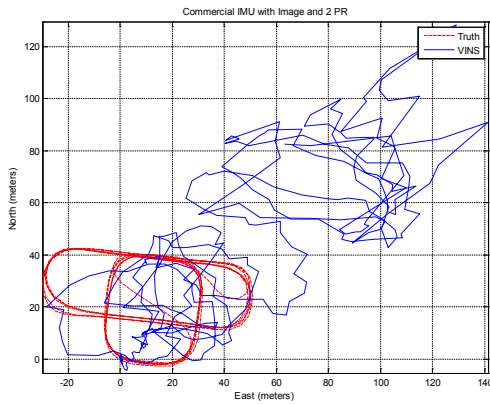


Side-Looking

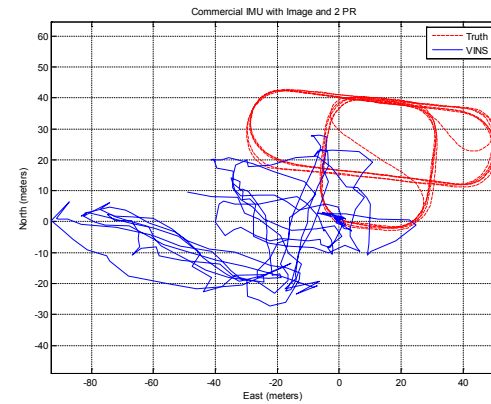


Forward-Looking

Figure 41. Comparison of Trajectories between Camera Pointing Directions (Scenario 2)

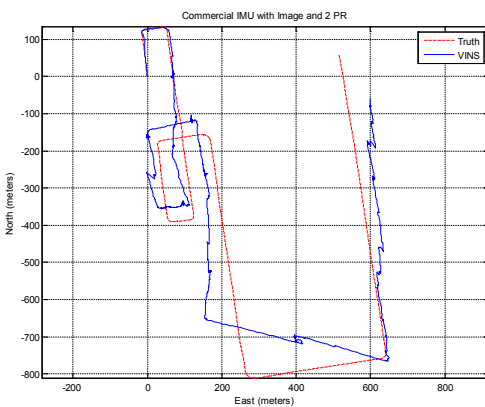


Side-Looking

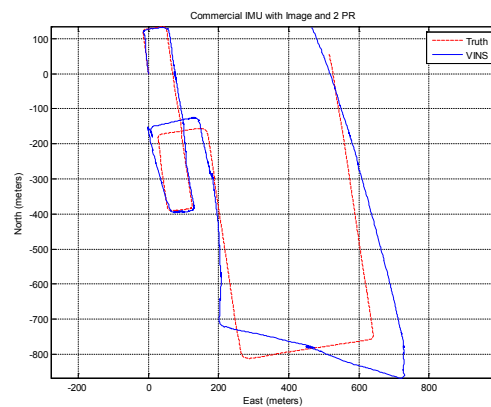


Forward-Looking

Figure 42. Comparison of Trajectories between Camera Pointing Directions (Scenario 6)



Side-Looking



Forward-Looking

Figure 43. Comparison of Trajectories between Camera Pointing Directions (Scenario 7)

4.2.6 Method of Calculating Direction of Translation.

The ZUPT measurements implemented in this thesis were dependent on how the direction of translation of the sensor was determined. There are two methods of doing this in a VINS. In the first method, the rotation of the sensor was determined by the IMU and this information was used to determine the direction of translation. This method, termed as ‘Cal t known R’ in this thesis, is novel as it coupled the measurements from an IMU to visual odometry. In the second method, both the rotation and translation of the sensor, termed as ‘Cal t and R’ in this thesis, were determined by visual odometry without any measurements from IMU. Both methods of calculating the direction of translation were implemented in the simulation platform and the results are shown in Table 12. In all 3 scenarios, ‘Cal t known R’ performed better than ‘Cal t and R’. It is postulated that the ‘Cal t known R’ method has better performance as this method took the rotation measurement from IMU and hence it was less susceptible to noise in the image measurements. Conversely, ‘Cal t and R’ was more susceptible to noise in the image measurements approximately 30% of the translations and rotations, calculated using this method, were assessed to be invalid as shown in Table 13. These invalid translations were not used as image measurements to update the VINS.

Table 12. Effects of Method of Calculating Direction of Translation on Accuracy of Position. The performance of ‘Cal t and R’ is compared to the performance of ‘Cal t known R’. A value that is more than 1 indicates a better performance for ‘Cal t and R’ while a value that is less than 1 indicates a worse performance for ‘Cal t and R’.

Scenario	DRMS - Cal t known R (m)	DRMS - Cal t and R (m)	Performance of ‘Cal t and R’ Compared to ‘Cal t known R’
2	77.0	219.9	0.35
6	43.7	96.9	0.45
7	80.3	513.6	0.15

Table 13. Number of Invalid Translation and Rotation with ‘Cal t and R’

Scenario	Number of Image Measurements	Number of Invalid Translation and Rotation	Percentage of Invalid Translation and Rotation (%)
2	1301	397	30.5
6	1018	345	33.9
7	2039	643	31.5

4.2.7 GPS Clock.

In areas of GPS outages, it might be possible for 3 or less GPS pseudorange measurements to be available. Although these pseudoranges could not be used to determine a navigation solution on its own, they could be used to improve the accuracy of a VINS as seen from Section 4.2.1. Table 14 shows the improvement in the position accuracy of a nominal VINS with different grades of GPS receiver clock. The Rubidium and Ovenised Crystal clocks performed 9% to 15% better than the Crystal clock. It was observed that the higher quality clock, Rubidium, did not give better improvement compared to Ovenised Crystal. A postulation for this observation was that the advantage of having a better clock does not materialize when there were fewer than 3 pseudorange measurements. Table 15 shows that with only 2 pseudorange measurements, the performance of an ovenised crystal GPS receiver clock is comparable to the performance of a Rubidium GPS receiver clock.

Table 14. Effects of Type of GPS Receiver Clock on Accuracy of Position (With Image and 2 Pseudorange Measurements)

GPS Receiver Clock	DRMS (m)	DRMS / Distance Travelled (%)	Performance Compared to Nominal
Crystal (nominal)	77.0	3.13	1
Ovenised Crystal	67.2	2.73	1.15
Rubidium	70.6	2.87	1.09

Table 15. Effects of Type of GPS Receiver Clock on Accuracy of Position (With 2 Pseudorange Measurements)

GPS Receiver Clock	DRMS (m)	DRMS / Distance Travelled (%)	Performance Compared to Crystal
Crystal	20969	851.18%	1
Ovenised Crystal	8858	359.57%	2.36
Rubidium	8338	338.46%	2.51

4.2.8 Number of Pseudorange Measurements.

As the VINS would be used in areas with GPS outages, the trade study focused mainly on the effects of having 3 or less pseudoranges from GPS. Table 16 shows the effects of the number of pseudorange measurements on position accuracy. A VINS with 3 or more pseudorange measurements would have an error of less than 1% over the distance travelled. However, this is not representative of a typical situation with GPS outage. It is more realistic for a VINS to receive not more than 2 pseudorange measurements in areas of GPS outage. In these situations, the advantage of having 2 pseudorange measurement is significant as the position accuracy improved by a factor of two compared to having 1 or no pseudorange measurements. Table 17 shows the benefits of incorporating image measurements when there are 3 or less pseudorange measurements, as the position accuracy improves by more than 38 times. The benefits of incorporating image measurements are less significant (approximately 1% improvement) when there are 4 or more pseudorange measurements.

Table 16. Effects of Number of Pseudoranges on Accuracy of Position (includes Image Measurements)

Number of Pseudoranges	DRMS (m)	DRMS / Distance Travelled (%)	Performance Compared to Nominal
0	183.8	7.46	0.42
1	155.3	6.30	0.50
2 (nominal)	77.0	3.13	1
3	4.2	0.17	18.17
4	3.1	0.13	24.69
8	1.8	0.07	44.02

Table 17. Effects of Number of Pseudoranges on Accuracy of Position (with Image Measurements and without Image Measurements)

Number of Pseudoranges	DRMS - With Image (m)	DRMS - Without Images (m)	Performance of “With Image” compared to “Without Image”
1	155.3	35730.0	230
2	77.0	20969.0	272
3	4.2	161.5	38
4	3.1	3.5	1.1
8	1.8	1.8	1

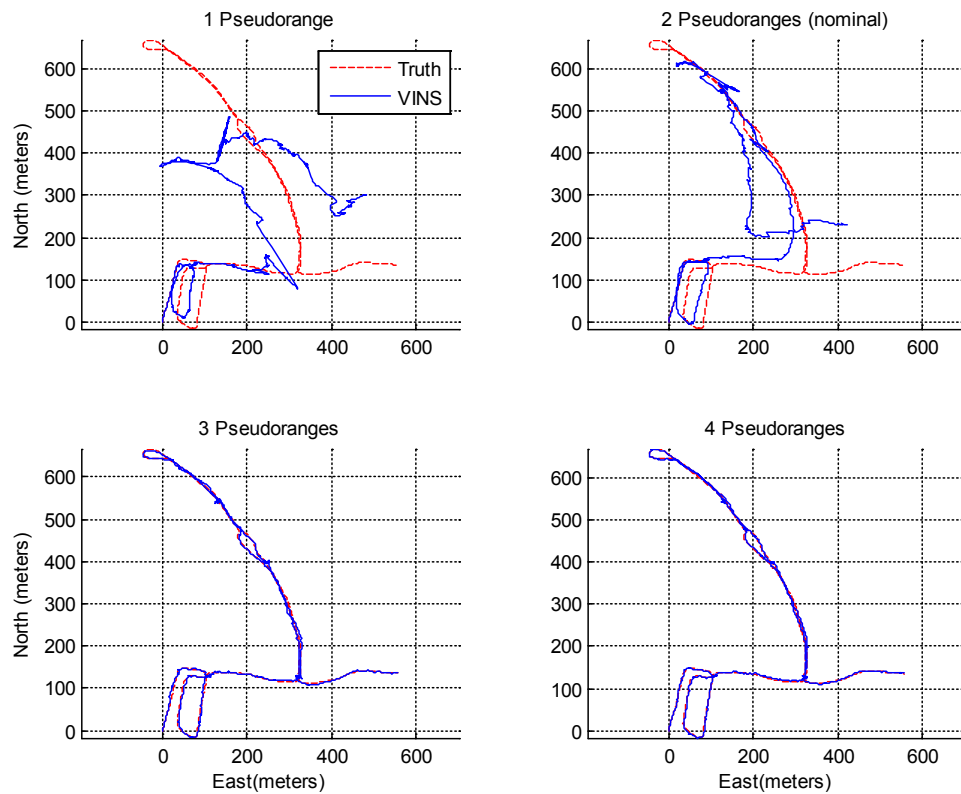


Figure 44. Comparison of Trajectories among Different Number of Pseudorange Measurements

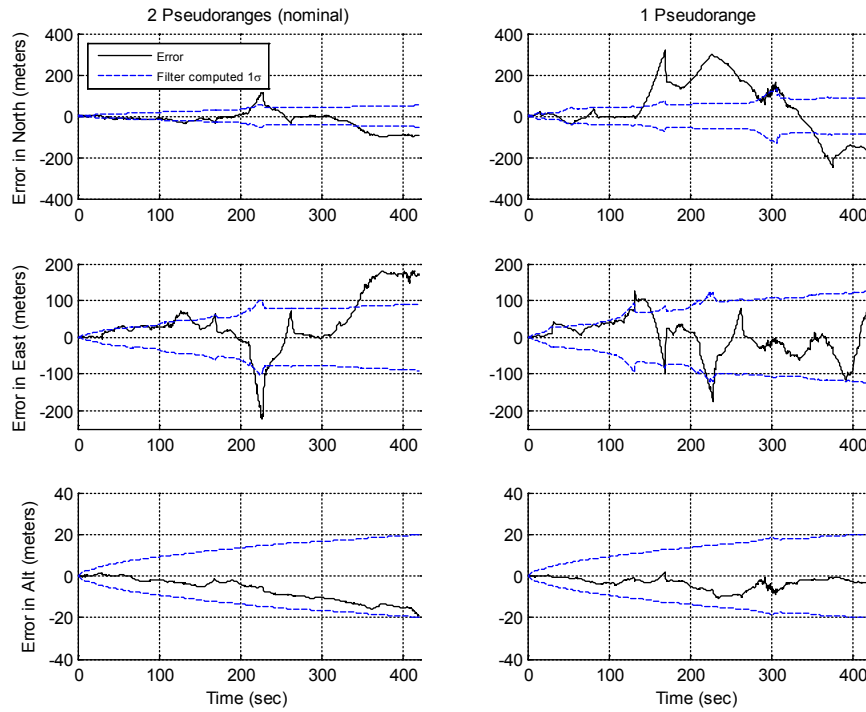


Figure 45. Comparison of Position Error (2 Pseudoranges vs 1 Pseudorange)

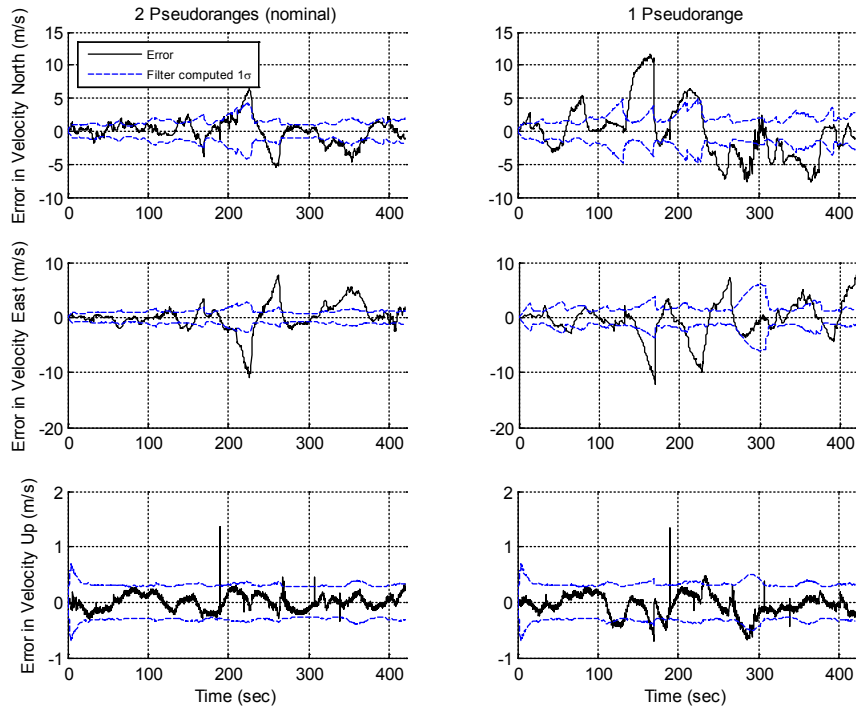


Figure 46. Comparison of Velocity Error (2 Pseudoranges vs 1 Pseudorange)

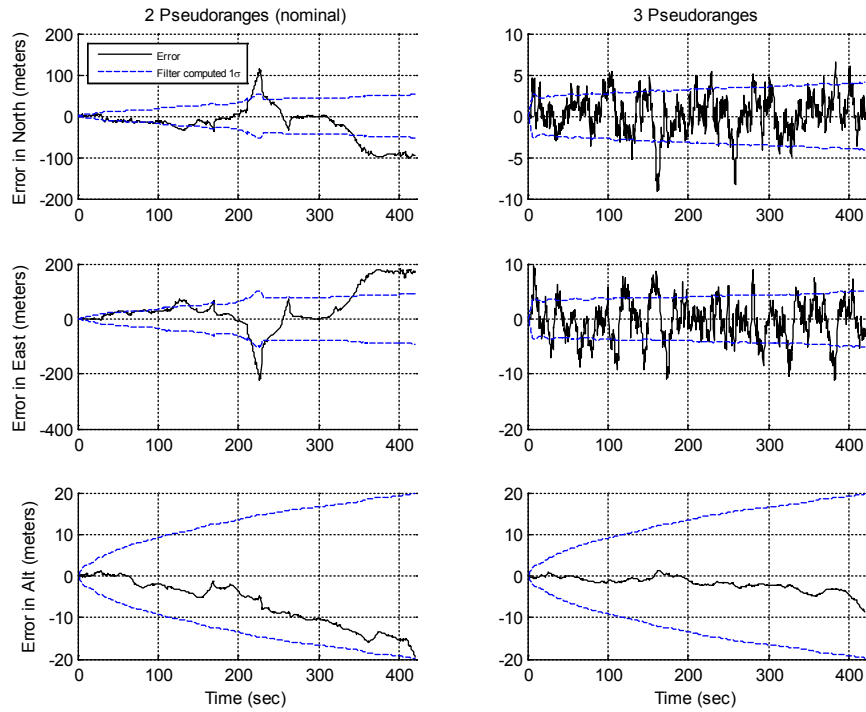


Figure 47. Comparison of Position Error (2 Pseudoranges vs 3 Pseudoranges)

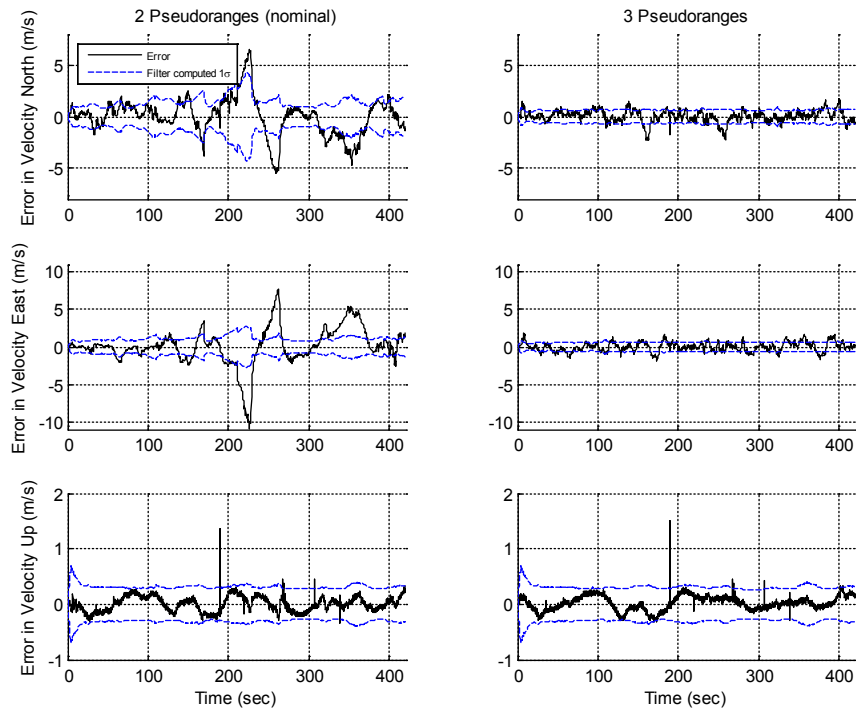


Figure 48. Comparison of Velocity Error (2 Pseudoranges vs 3 Pseudoranges)

4.3 Conclusion from Trade Study

Results from the trade study confirmed that in an area with limited GPS signals, the performance of a VINS (commercial grade INS integrated with visual odometry and GPS pseudorange measurements) is better than an INS that is integrated with either visual odometry or GPS pseudorange. The trade study also revealed the trade-off in the performance of a VINS as a function of its update interval, IMU quality, camera quality and camera pointing direction.

4.4 Summary

The simulation platform developed in this research was used to carry out a trade study on the design of a VINS. This demonstrated the utility of the platform in the development and evaluation of a VINS.

V. Conclusions and Recommendations

This chapter concludes the research and highlights its significance. Thereafter, recommendations are also made for future work.

5.1 Conclusions of Research

This research successfully developed a simulation platform using real-world images and PVA data collected from a ground vehicle as part of the ASPN program. The simulation platform was built using Matlab. It met all the requirements stated in Table 1 and is capable of simulating a VINS operating in an environment with limited GPS signals. A trade study on the design of a VINS demonstrated the utility of the platform and the key findings were:

- In an environment with limited GPS signals, an INS that incorporated both image and GPS pseudorange measurements performed better than an INS that incorporated either image or GPS pseudorange measurements by themselves.
- Among the different grades of IMU, the benefit of incorporating image and GPS pseudorange measurements was most significant for a commercial grade IMU. The benefit was negligible for a navigation grade IMU for the scenarios tested.
- Despite additional matched features that a forward-looking camera was able to pick up compared to a side-looking camera, the performance of a VINS that incorporated a forward-looking camera was only slightly better than that of a VINS that incorporated a side-looking camera.
- The quality of GPS clock had minimal effect on the performance of a VINS when there were fewer than 3 pseudorange measurements.

- A VINS with image and 3 pseudorange measurements has similar performance to an INS with no image and 4 pseudorange measurements.

5.2 Significance of Research

The development of a VINS requires a significant amount of effort for performance tuning, verification and validation. The simulation platform, developed in this research, would allow future researchers to test the design of a VINS in various simulated environments prior to physical testing of the system in a real environment. Such simulations allow researchers to focus on the design of navigation filters for a VINS while eliminating hardware and data synchronization problems.

5.3 Recommendations for Future Research

The following recommendations on future research areas are proposed based on the experiences gained in this research.

5.3.1 Alternate Filter Implementation.

There are many options for integration of INS, visual odometry and GPS pseudoranges in a VINS. This research used a basic Kalman filter to integrate these measurements. The simulation platform could be modified to implement an advanced navigation filter and to model a more complex VINS. This would further exploit the benefits of integrating visual odometry with INS, and would yield additional improvements in performance.

5.3.2 Implement Delayed State Update Equation.

For simplification, this research did not implement a delayed-state update equation for the zero velocity update. Hence, results from the simulation platform were

not as accurate as it could be. A delayed-state update equation could be implemented in future research to improve the operation and performance of the simulation platform.

5.3.3 Using Design of Experiment for Trade Space Analysis.

This research made use of the trade space analysis to demonstrate the utility of the simulation platform. A couple of postulations were made to explain some of the results observed. Future research could carry out a more thorough and systematic analysis of the trade space by using the design of experiment approach. This would provide results that are better substantiated.

5.3.4 Implement Altitude Aiding.

This research did not implement any form of altitude aiding for the VINS. As it is fairly common for INS to have altitude aiding, future research could study the benefits of including altitude aiding in a VINS.

Bibliography

- Bonarini, A., Burgard, W., Fontana, G., Matteucci, M., Sorrenti, D. G. & Tardos, J. D. (2014). RAWSEEDS: Robotics Advancement through Web-publishing of Sensorial and Elaborated Extensive Data Sets. 11 August 2014
<http://www.rawseeds.org/home/>
- Brown, R. G., & Hwang, P. Y. (1992). *Introduction to Random Signals and Applied Kalman Filtering* (2nd ed.). New York: John Wiley & Son.
- Chowdhary, G., Johnson, E. N., Magree, D., Wu, A., & Shein, A. (2013). "GPS-Denied Indoor and Outdoor Monocular Vision Aided Navigation and Control of Unmanned Aircraft," *Journal of Field Robotics*, 30(3), 415-438.
- Dae Hee Won, Sukchang Yun, Young Jae Lee, & Sangkyung Sung. (2012). "Integration of Limited GNSS Signals with Monocular Vision Based Navigation," 12th *International Conference on Control, Automation and Systems (ICCAS)*. 1364-1367.
- George, M., & Sukkarieh, S. (2007). "Camera Aided Inertial Navigation in Poor GPS Environments," *2007 IEEE Aerospace Conference*. 1-12.
- Giebner, M. G. (2003). *Tightly-Coupled Image-Aided Inertial Navigation System via a Kalman Filter*. MS thesis, AFIT/GE/ENG/03-10. Graduate School of Engineering and Management, Air Force Institute of Technology (AU), Wright-Patterson AFB OH, March 2003 (ADA415246).
- Hartley, R., & Zisserman, A. (2004). *Multiple View Geometry in Computer Vision* (2nd ed.). New York: Cambridge University Press.
- Kauffman, K., Morton, Y., Raquet, J., & Garmatyuk, D. (2011). "Simulation Study of UWB-OFDM SAR for Navigation with INS Integration," *Proceedings of the 2011 International Technical Meeting of the Institute of Navigation*.
- Longuet-Higgins, H. C. (1987). "A Computer Algorithm for Reconstructing a Scene from Two Projections," *Readings in Computer Vision: Issues, Problems, Principles, and Paradigms*. 61-62.
- Lowe, D. G. (1999). "Object Recognition from Local Scale-Invariant Features," *The Proceedings of the Seventh IEEE International Conference on Computer Vision*. 1150-1157.
- Lowe, D.G. (2004). "Distinctive image features from scale-invariant keypoints," *International Journal of Computer Vision*, 91-110.

- Misra, P., & Enge, P. (2006). *Global Positioning System: Signals, Measurements and Performance Second Edition*. Lincoln, MA: Ganga-Jamuna Press.
- National Imagery and Mapping Agency. (2004). *Department of Defense World Geodetic System 1984. Its Definition and Relationships with Local Geodetic Systems*. (No. NIMA TR8350.2 3rd Edition). Springfield VA: National Imagery and Mapping Agency.
- Noureldin, A., Karamat, T. B., & Georgy, J. (2013). *Fundamentals of Inertial Navigation, Satellite-Based Positioning and their Integration*. New York: Springer Berlin Heidelberg.
- Raquet, J. (2014). Course handout. *Vision-Aided Navigation*. Consortium of Ohio Universities on Navigation and Timekeeping (COUNT) Annual Short Course.
- Seong-Baek Kim, Seung-Yong Lee, Tae-Hyun Hwang, & Kyoung-Ho Choi. (2004). "An Advanced Approach for Navigation and Image Sensor Integration for Land Vehicle Navigation," *IEEE 60th Vehicular Technology Conference*. 4075-4078.
- Technische Universität München. (2014). RGB-D SLAM Dataset and Benchmark. 11 August 2014 <http://vision.in.tum.de/data/datasets/rgbd-dataset/download>
- University of Southern California Robotics Research Lab. (2011). Radish: The Robotics Data Set Repository. 11 August 2014 <http://cres.usc.edu/radishrepository/view-all.php>
- Veth, M. J. (2006). *Fusion of Imaging and Inertial Sensors for Navigation*. PhD dissertation. Air Force Institute of Technology (AU), Wright-Patterson AFB OH, September 2006. (ADA468382).
- Veth, M., & Raquet, J. (2007). *Fusion of Low-cost Imaging and Inertial Sensors for Navigation*.

REPORT DOCUMENTATION PAGE				Form Approved OMB No. 0704-0188	
<p>The public reporting burden for this collection of information is estimated to average 1 hour per response, including the time for reviewing instructions, searching existing data sources, gathering and maintaining the data needed, and completing and reviewing the collection of information. Send comments regarding this burden estimate or any other aspect of the collection of information, including suggestions for reducing this burden to Department of Defense, Washington Headquarters Services, Directorate for Information Operations and Reports (0704-0188), 1215 Jefferson Davis Highway, Suite 1204, Arlington, VA 22202-4302. Respondents should be aware that notwithstanding any other provision of law, no person shall be subject to a penalty for failing to comply with a collection of information if it does not display a currently valid OMB control number.</p> <p>PLEASE DO NOT RETURN YOUR FORM TO THE ABOVE ADDRESS.</p>					
1. REPORT DATE (DD-MM-YYYY)		2. REPORT TYPE		3. DATES COVERED (From – To)	
18-09-2014		Master's Thesis		Sep 2013 – Sep 2014	
4. TITLE AND SUBTITLE Simulation Platform for Vision Aided Inertial Navigation				5a. CONTRACT NUMBER	
				5b. GRANT NUMBER	
				5c. PROGRAM ELEMENT NUMBER	
6. AUTHOR(S) Png, Jason. Military Expert 5 (Major), Republic of Singapore Air Force				5d. PROJECT NUMBER	
				5e. TASK NUMBER	
				5f. WORK UNIT NUMBER	
7. PERFORMING ORGANIZATION NAMES(S) AND ADDRESS(S) Air Force Institute of Technology Graduate School of Engineering and Management (AFIT/EN) 2950 Hobson Way WPAFB OH 45433-7765				8. PERFORMING ORGANIZATION REPORT NUMBER AFIT-ENV-T-14-S-14	
9. SPONSORING/MONITORING AGENCY NAME(S) AND ADDRESS(ES) AGENCY (spelled out) Dr Adam J Rutkowski AFRL / RWWI 101 West Eglin Blvd Eglin AFB, FL 32542 (850) 875-2632, adam.rutkowski@us.af.mil				10. SPONSOR/MONITOR'S ACRONYM(S) AFRL / RWWI	
				11. SPONSOR/MONITOR'S REPORT NUMBER(S)	
12. DISTRIBUTION/AVAILABILITY STATEMENT DISTRIBUTION STATEMENT A. APPROVED FOR PUBLIC RELEASE; DISTRIBUTION UNLIMITED.					
13. SUPPLEMENTARY NOTES This material is declared a work of the U.S. Government and is not subject to copyright protection in the United States.					
14. ABSTRACT Integrated Inertial Navigation System (INS) and Global Positioning System (GPS) solutions have become the backbone of many modern positioning and navigation systems. The Achilles' heel of such systems are their susceptibility to GPS outages. Hence, there has been sustained interest in alternate navigation techniques to augment a GPS/INS system. With the advancement in camera technologies, visual odometry is a suitable technique. As the cost and effort required to conduct physical trials on a visual odometry system is extensive, this research seeks to provide a simulation platform that is capable of simulating different grades of GPS/INS systems under various realistic visual odometry scenarios. The simulation platform also allows standardized data to be tested across different navigation filters. The utility of this simulation platform is demonstrated by a trade study on factors affecting the performance of a GPS/INS system augmented with visual odometry.					
15. SUBJECT TERMS Vision-aided Inertial Navigation System. Visual odometry. Simulation Platform. Trade Study.					
16. SECURITY CLASSIFICATION OF:			17. LIMITATION OF ABSTRACT UU	18. NUMBER OF PAGES 93	19a. NAME OF RESPONSIBLE PERSON Dr David R. Jacques, AFIT/ENV
a. REPORT U	b. ABSTRACT U	c. THIS PAGE U			19b. TELEPHONE NUMBER (Include area code) (937) 255-6565, ext 3329 (David.Jacques@afit.edu)

Standard Form 298 (Rev. 8-98)
Prescribed by ANSI Std. Z39-18